Editors' Suggestion

Giant effective magnetic moments of chiral phonons from orbit-lattice coupling

Swati Chaudhary,[1,2,3,*] Dominik M. Juraschek,[4] Martin Rodriguez-Vega,[1,2] and Gregory A. Fiete[2,3]

[1]*Department of Physics, The University of Texas at Austin, Austin, Texas 78712, USA*

[2]*Department of Physics, Northeastern University, Boston, Massachusetts 02115, USA*

[3]*Department of Physics, Massachusetts Institute of Technology, Cambridge, Massachusetts 02139, USA*

[4]*School of Physics and Astronomy, Tel Aviv University, Tel Aviv 6997801, Israel*

(Received 26 October 2023; revised 3 August 2024; accepted 7 August 2024; published 3 September 2024)

Circularly polarized lattice vibrations carry angular momentum and lead to magnetic responses in applied magnetic fields or when resonantly driven with ultrashort laser pulses. Recent measurements have found responses that are orders of magnitude larger than those calculated in prior theoretical studies. Here, we present a microscopic model for the effective magnetic moments of chiral phonons in magnetic materials that can reproduce the experimentally measured magnitudes and that allows us to make quantitative predictions for materials with giant magnetic responses using microscopic parameters. Our model is based on orbit-lattice couplings that hybridize optical phonons with orbital electronic transitions. First, we test our model by applying it to $4f$ rare-earth halide paramagnets, which are known to exhibit a giant phonon Zeeman effect. Next, we predict that this effect can also occur for optical phonons in $3d$ transition-metal oxide magnets. We show that the nature of low-energy excitations involved in phonon hybridization is remarkably different than that of rare-earth systems. The temperature trend of phonon magnetic moment in d-orbital magnets also reveals valuable insights about the magnetic ground state and the unique interplay of spin, orbital, and lattice degree of freedom. In both cases, we find that chiral phonons can carry giant effective magnetic moments of the order of a Bohr magneton, orders of magnitude larger than previous predictions.

DOI: 10.1103/PhysRevB.110.094401

I. INTRODUCTION

Circularly polarized lattice vibrations, also called chiral phonons, lead to orbital motions of the atoms in a crystal, producing angular momentum [1–5]. In an ionic lattice, the orbital motions of the ions create atomistic circular charge currents and therefore produce a collective phonon magnetic moment [6–9]. Phonon magnetic moments lead to magnetic responses when an external magnetic field is applied or when they are resonantly excited with an ultrashort terahertz pulse. In an applied static magnetic field, the frequencies between right- and left-handed circular polarizations split, which is known as the phonon Zeeman effect [7,8,10–13], and propagating phonons with opposite chirality are deflected in different directions, which is known as the phonon Hall effect [14–22]. If the chiral phonons are infrared active, they can be resonantly excited with an ultrashort terahertz or mid-infrared pulse, which generates a macroscopic phonon magnetic moment and therefore effective magnetic field, a phenomena that has become known as the phonon inverse Faraday or phonon Barnett effect in recent studies [7,8,23–34]. The angular momentum carried by chiral phonons can be transferred to the electrons, leading to different spin-polarized phenomena without any external magnetic field [35–37].

The phonon magnetic moment produced by an ionic charge current scales with the gyromagnetic ratio of the ions, $\gamma = Z^*/(2M)$, which depend on the effective ionic charge Z^* and the ionic mass M. Previous studies based on density functional theory have computed phonon magnetic moments in various nonmagnetic materials to yield values of up to a nuclear magneton [7,8,12,27,38,39]. Intriguingly, a number of early and recent experiments have measured large magnitudes of phonon Zeeman effects in paramagnets [40,41] and in materials with nontrivial electronic band geometries [10,11,42,43] that suggest the presence of phonon magnetic moments ranging from fractions of to a few Bohr magnetons, several orders of magnitude larger than the nuclear magneton. Furthermore, very recent pump-probe experiments have shown that coherently driven chiral phonons produce magnetizations in nonmagnetic materials [30] and paramagnets [31,32] that are compatible with phonon magnetic moments on the Bohr-magneton scale. These findings indicate that the phonon magnetic moment contains additional contributions from electron-phonon or spin-phonon coupling that allow it to reach the order of a Bohr magneton.

Theories based on electron-phonon coupling have so far involved two types of explanations for materials with nontrivial electronic band topology: First, an adiabatic evolution of the electronic states alongside the circularly polarized phonon modes that induces an adiabatic electronic orbital magnetization [44–47], and second, a coupling of the cyclotron motion of electrons close to a Dirac point to the chiral phonon mode [10]. Theories based on spin-phonon coupling have focused both on nonmagnetic and paramagnetic materials: In paramagnets, phonon modes can couple to the electron spin through modifications of the crystal electric field (CEF) and subsequently through the spin-orbit coupling [26,48,49]. For nonmagnetic materials, a recent proposal suggests that the spin channels of doping-induced conduction electrons couple

*Contact author: swati.chaudhary@austin.utexas.edu

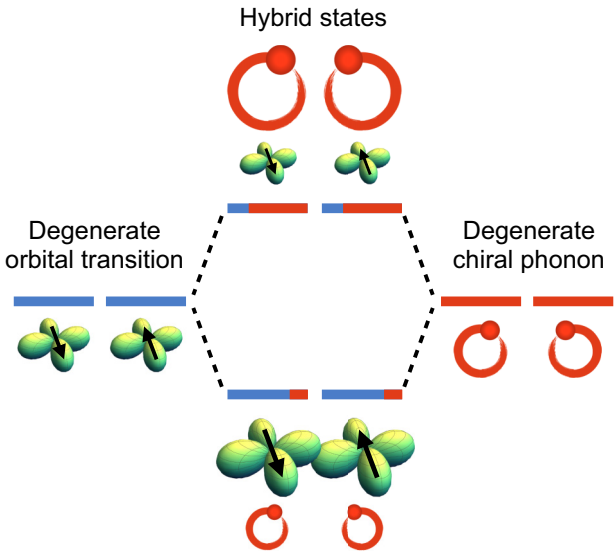

FIG. 1. Orbit-lattice coupling of chiral phonons. A degenerate chiral phonon mode couples to a degenerate orbital transition and forms two hybridized branches, one with primarily phonon contribution and one with primarily orbital contribution. The chiral phonon mode therefore obtains part of the g factor from the orbital transition, which is orders of magnitude larger than its own.

to the phonon magnetic moment, resulting in phonon-induced electronic polarization [29,33]. Despite these developments, a microscopic theory that can quantitatively predict the experimentally found giant effective magnetic moments of phonons is still missing.

Here, we develop a microscopic model for effective phonon magnetic moments in paramagnetic and magnetic materials. Our model is based on electron-phonon coupling, and more specifically orbit-lattice coupling, which leads to a hybridization of degenerate chiral phonon modes and degenerate orbital excitations, as illustrated in Fig. 1. We perform a comprehensive group-theoretical analysis to identify the possible couplings between chiral phonon modes and orbital transitions and apply it to two distinct cases: First, to the case of $4f$ paramagnetic rare-earth trihalides, in which the spin-orbit splitting is much larger than the CEF splitting. In these materials, a CEF excitation hybridizes with doubly degenerate phonons, which allows them to obtain a large phonon magnetic moment. Here, our model is able to quantitatively predict the giant phonon Zeeman splittings that were measured already half a century ago [40,41], using only microscopic parameters in combination with results from first-principles calculations. Second, our model predicts that a phonon Zeeman effect can also occur in $3d$ magnets, where the CEF splitting of the e_g and t_{2g} orbitals is much larger than the spin-orbit splitting. In $3d$-orbital systems, the hybridization occurs between doubly degenerate phonons and orbital excitations connecting multiplets that are split by the spin-orbit coupling or by lattice distortions. We predict that this mechanism can lead to large effective phonon magnetic moments and therefore phonon Zeeman splittings when the energies of the orbital transitions and the phonons become comparable.

II. PHONON ZEEMAN SPLITTING AND EFFECTIVE PHONON MAGNETIC MOMENT

In this section, we discuss a detailed microscopic model for the Zeeman splitting of doubly degenerate phonon modes at or near the center of the Brillouin zone. The doubly degenerate phonon modes hybridize with orbital transitions between Kramers doublets on a magnetic ion, and their frequencies split when the degeneracy of the Kramers doublets is lifted by an external magnetic field. This model builds on the early work of Ref. [48] and can be described by the Hamiltonian

$$H = H_{el} + H_{ph} + H_{el-ph}. \tag{1}$$

Here, H_{el} describes the electronic states of the magnetic ion, H_{ph} is the Hamiltonian of a doubly degenerate phonon mode, and H_{el-ph} describes the electron-phonon coupling. We consider a magnetic ion with doubly degenerate electronic levels (Kramers doublets), which are eigenstates of the total electronic angular momentum J and are split in energy by the CEF or spin-orbit coupling. The electronic Hamiltonian can therefore be written as

$$H_{el} = \sum_i \varepsilon_i \left|\psi_i\right\rangle \left\langle\psi_i\right|, \tag{2}$$

where ε_i is the energy of state i. These states are given by the ground-state and excited-state Kramers doublets, and we will look at two Kramers doublets at a time. We denote the states of the ground-state doublet by

$$\left|\psi_1\right\rangle = \left|J = J_\alpha, m_j = m_j^\alpha\right\rangle, \tag{3}$$

$$\left|\psi_2\right\rangle = \left|J = J_\alpha, m_j = -m_j^\alpha\right\rangle, \tag{4}$$

and those of the excited-state doublet by

$$\left|\psi_3\right\rangle = \left|J = J_\beta, m_j = m_j^\beta\right\rangle, \tag{5}$$

$$\left|\psi_4\right\rangle = \left|J = J_\beta, m_j = -m_j^\beta\right\rangle. \tag{6}$$

In the absence of a magnetic field, $\varepsilon_1 = \varepsilon_2$ and $\varepsilon_3 = \varepsilon_4$.

The Hamiltonian of a doubly degenerate phonon mode consisting of the orthogonal components a and b is given by

$$H_{ph} = \omega_0 (a^\dagger a + b^\dagger b). \tag{7}$$

Here, ω_0 is the eigenfrequency of the doubly degenerate phonon mode. We set $\hbar = 1$ and treat frequencies and energies equivalently in the following. $a^\dagger, b^\dagger$ (a, b) are the bosonic creation (annihilation) operators of the two orthogonal components. These phonons can interact with the electronic states of the magnetic ion and mix different Kramers doublets. The electron-phonon coupling is therefore given by an orbit-lattice coupling, originating from the modification of the crystal electric field by the lattice vibrations. It can be obtained by expanding the crystal field to first order in the atomic displacements along the eigenvectors of a phonon mode and can be written as

$$H_{el-ph} = \sum_{\Gamma_\alpha} Q_{\Gamma_\alpha} \widehat{\mathbf{O}}_{\Gamma_\alpha}, \tag{8}$$

where $\widehat{\mathbf{O}}_{\Gamma_\alpha}$ is an operator acting on the electronic states and Q_{Γ_α} is the displacement associated with phonon mode α with irreducible representation Γ. For pure CEF excitations, where

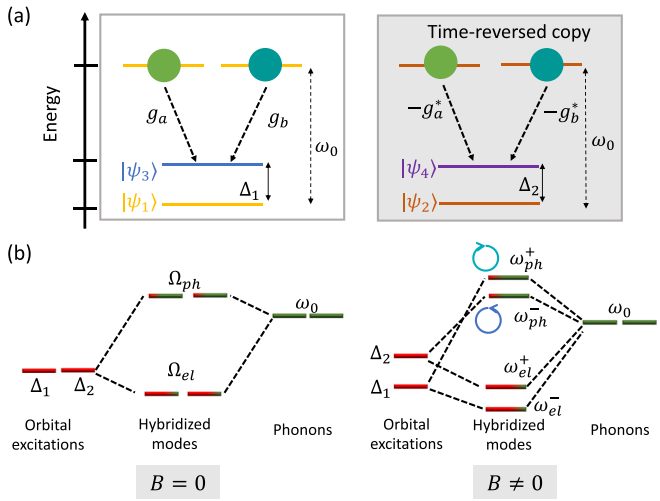

FIG. 2. Splitting of chiral phonons in a magnetic field through orbit-lattice coupling. (a) (Left) The two components, a and b (green spheres), of a doubly degenerate phonon with frequency ω_0 couple to the orbital transition between the ground and excited CEF states, ψ_1 and ψ_3, with frequency Δ_1. The coupling strengths are given by g_a and g_b. (Right) The time-reversal partners of the states on the left also couple to the two components of this phonon. When time-reversal symmetry is preserved, states ψ_1 and ψ_2 are degenerate, as well as ψ_3 and ψ_4, and therefore $\Delta_1 = \Delta_2$. (b) (Left) Energy level diagram of the coupling between the orbital transitions, Δ_1 and Δ_2, and a doubly degenerate phonon, ω_0, forming hybrid orbit-lattice modes, Ω_{ph} and Ω_{el}, with mainly phononic and electronic admixtures respectively. The phonon frequencies are renormalized, but remain degenerate. (Right) A magnetic field lifts the degeneracy of the orbital transitions, Eq. (23), and therefore the degeneracy of the hybrid modes. The hybrid states with mainly phonon admixture can be seen as circularly polarized phonon states with frequencies $\omega_{ph}^{\pm}$.

both doublets belong to the same multiplet, these operators take the form of Steven's operators [50], but we keep it more general here to also include the possibility to describe spin-orbit excitations. In our microscopic model, these operators are computed from the changes of the Coulomb potential around the magnetic ion, where we treat all ions as point charges. We ignore higher-order corrections in the lattice displacement, which would lead to higher-order scattering processes that are not considered here. Within this expansion, the orbit-lattice coupling term can be written as

$$H_{el-ph} = (a^\dagger + a)\widehat{\mathbf{O}}_a + (b^\dagger + b)\widehat{\mathbf{O}}_b, \tag{9}$$

where $\widehat{\mathbf{O}}_{a/b}$ can couple different electronic states. The form of these operators is determined by time-reversal symmetry and can be expressed as

$$\widehat{\mathbf{O}}_a = g_a\,|\psi_1\rangle\langle\psi_3| - g_a^*\,|\psi_2\rangle\langle\psi_4| + \text{H.c.}, \tag{10}$$

$$\widehat{\mathbf{O}}_b = g_b\,|\psi_1\rangle\langle\psi_3| - g_b^*\,|\psi_2\rangle\langle\psi_4| + \text{H.c.} \tag{11}$$

where the values of $g_{a/b}$ depend on the strength of the orbit-lattice coupling. The couplings of the phonons to the electronic states are illustrated in Fig. 2(a).

There are further coupling terms that mix the states ψ_1 and ψ_4, as well as ψ_2 and ψ_3, which in most cases turn out to be zero, however. Heuristically, this can be understood on the basis of angular momentum transfer. The chiral superposition of two components of a doubly degenerate mode possesses angular momentum $\pm l\hbar$ and thus only mixes electronic states for which the change in angular momentum is given by $|\Delta m_j| = l$. This restricts the number of terms in Eq. (11), and it thus suffices to take into consideration only the transitions between ψ_1 and ψ_3 as well as ψ_2 and ψ_4. We will discuss the explicit form of this mixing for each of the examples in Secs. III and IV.

The electron-phonon interaction therefore manifests as orbit-lattice coupling and hybridizes phonons and electronic excitations, which modifies the phonon frequencies. The modification of the phonon spectrum can be obtained using a Green's-function formalism. For the noninteracting case, described by H_{ph}, the bare phonon Green's function is given by

$$\mathbf{D}_0(\omega) = \begin{pmatrix} D_0^{aa}(\omega) & 0 \\ 0 & D_0^{bb}(\omega) \end{pmatrix}, \tag{12}$$

where $D_0^{aa}(\omega) = D_0^{bb}(\omega) = \frac{2\omega_0}{\omega^2 - \omega_0^2}$, and the phonon energies are trivially retrieved by solving $\text{Det}(\mathbf{D}_0^{-1}(\omega)) = 0$. Including interactions, the full phonon Green's function is given by

$$\mathbf{D}^{-1}(\omega) = \mathbf{D}_0^{-1}(\omega) - \mathbf{\Pi}(\omega), \tag{13}$$

where the phonon self-energy matrix $\mathbf{\Pi}(\omega)$ contains corrections from the orbit-lattice coupling. The leading-order corrections are given by

$$\Pi^{aa} = 4\pi\,|g_a|^2\left(\frac{f_{13}\varepsilon_{13}}{\omega^2 - \varepsilon_{31}^2} + \frac{f_{24}\varepsilon_{24}}{\omega^2 - \varepsilon_{42}^2}\right), \tag{14}$$

$$\Pi^{bb} = 4\pi\,|g_b|^2\left(\frac{f_{13}\varepsilon_{13}}{\omega^2 - \varepsilon_{31}^2} + \frac{f_{24}\varepsilon_{24}}{\omega^2 - \varepsilon_{42}^2}\right), \tag{15}$$

$$\Pi^{ab} = (\Pi^{ba})^* = \Pi^{ab}_{\text{Re}} + i\Pi^{ab}_{\text{Im}}. \tag{16}$$

The real and imaginary parts of the mixed term Π^{ab} are given by

$$\Pi^{ab}_{\text{Re}} = 4\pi\,\text{Re}(g_a g_b^*)\left(\frac{f_{13}\varepsilon_{13}}{\omega^2 - \varepsilon_{31}^2} + \frac{f_{24}\varepsilon_{24}}{\omega^2 - \varepsilon_{42}^2}\right), \tag{17}$$

$$\Pi^{ab}_{\text{Im}} = 4\pi\,\text{Im}(g_a g_b^*)\left(\frac{f_{13}\omega}{\omega^2 - \varepsilon_{31}^2} - \frac{f_{24}\omega}{\omega^2 - \varepsilon_{42}^2}\right), \tag{18}$$

$$\Pi^{ab} = 2\pi\left(\frac{g_a g_b^* f_{13}}{\omega - \varepsilon_{13}} - \frac{g_a^* g_b f_{13}}{\omega - \varepsilon_{31}} + \frac{g_a^* g_b f_{24}}{\omega - \varepsilon_{24}} - \frac{g_a g_b^* f_{24}}{\omega - \varepsilon_{42}}\right). \tag{19}$$

Here, $\varepsilon_{ij} = \varepsilon_i - \varepsilon_j$ is the energy difference between the states i and j and $f_{ij} = f_i - f_j$ is the difference in their occupancies, which are given by Fermi-Dirac distributions.

All of these terms in the self-energy matrix introduce corrections to the phonon energies. The phonon degeneracy can be lifted if the two diagonal terms are unequal. Eq. (13)

therefore becomes

$$\mathbf{D}^{-1}(\omega)=\begin{pmatrix}\frac{\omega^2-\omega_0^2}{2\omega_0}-\tilde{g}^2\left(\frac{f_1\Delta_1}{\omega^2-\Delta_1^2}+\frac{f_2\Delta_2}{\omega^2-\Delta_2^2}\right) & i\tilde{g}^2\left(-\frac{f_1\omega}{\omega^2-\Delta_1^2}+\frac{f_2\omega}{\omega^2-\Delta_2^2}\right)\\ -i\tilde{g}^2\left(-\frac{f_1\omega}{\omega^2-\Delta_1^2}+\frac{f_2\omega}{\omega^2-\Delta_2^2}\right) & \frac{\omega^2-\omega_0^2}{2\omega_0}-\tilde{g}^2\left(\frac{f_1\Delta_1}{\omega^2-\Delta_1^2}+\frac{f_2\Delta_2}{\omega^2-\Delta_2^2}\right)\end{pmatrix}, \tag{20}$$

where we redefine $\tilde{g}^2\equiv 4\pi g^2$, $\Delta_1\equiv\varepsilon_{31}$, $\Delta_2\equiv\varepsilon_{42}$, and we assume the excited-state Kramers doublet to be unoccupied, $f_3=f_4=0$. Please see the Appendix for a detailed derivation of Eq. (20). The leading-order corrections to the off-diagonal elements arise from the orbital transitions shown in Fig. 2(a) and can be understood in terms of the Feynman diagrams shown in Fig. 3.

With no external magnetic field applied, the occupancies of states 1 and 2 are equal, $f_1=f_2\equiv f_0/2$, (f_0 being the occupancy of the ground-state manifold), as well as the energies of both transitions, $1\to 3$ and $2\to 4$, $\Delta_1=\Delta_2\equiv\Delta$. Under these conditions, the two contributions shown in the two panels of Fig. 2(a) are equal in magnitude and opposite in sign, and thus the off-diagonal terms of the self-energy matrix vanish. As a result, phonons and electronic excitations hybridize to form doubly degenerate states with primarily electronic character and lower energies, and states with primarily phononic character and higher energies, as illustrated in Fig. 2(b) for $B=0$. We solve $\mathrm{Det}(\mathbf{D}^{-1}(B=0))=0$ to obtain the frequencies of the hybridized states with primarily phononic and electronic character, Ω_{ph} and Ω_{el},

$$\Omega_{ph}\equiv\omega_{ph}(B=0)=\left(\frac{\omega_0^2+\Delta^2}{2}+\sqrt{\left(\frac{\omega_0^2-\Delta^2}{2}\right)^2+2\tilde{g}^2f_0\omega_0\Delta}\right)^{1/2}, \tag{21}$$

$$\Omega_{el}\equiv\omega_{el}(B=0)=\left(\frac{\omega_0^2+\Delta^2}{2}-\sqrt{\left(\frac{\omega_0^2-\Delta^2}{2}\right)^2+2\tilde{g}^2f_0\omega_0\Delta}\right)^{1/2}. \tag{22}$$

The energy levels are depicted schematically in Fig. 2(b).

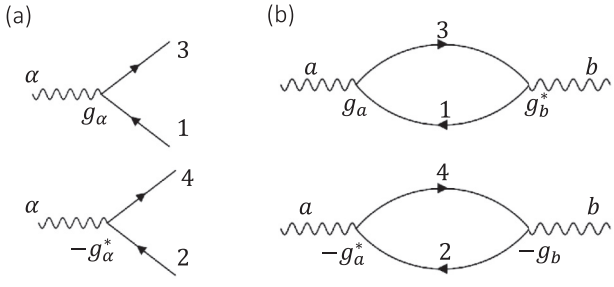

FIG. 3. Scattering mechanism of electron-phonon interactions. (a) Electron-phonon interaction vertices for a doubly degenerate phonon mode, $\alpha=(a,b)$, as defined by Eqs. (10) and (11). (b) Feynman diagrams representing the off-diagonal contributions to the phonon self-energy matrix, mixing the two orthogonal components, a and b, of the doubly degenerate phonon mode.

We next apply an external magnetic field, $\mathbf{B}=B\hat{\mathbf{z}}$, which lifts the degeneracies of the Kramers doublets, $\varepsilon_{12}\neq 0$ and $\varepsilon_{34}\neq 0$. This subsequently modifies the electronic transition energies according to

$$\Delta_1=\Delta-\gamma B,\quad \Delta_2=\Delta+\gamma B, \tag{23}$$

where $\gamma=\mu_{ex}^{el}-\mu_{gs}^{el}=(g_{ex}^{el}-g_{gs}^{el})\mu_B$ contains the g factors of the ground- and excited-state doublets. Lifting the degeneracy of the ground-state doublet leads to an asymmetric population of the ground-state energy levels, $f_{12}\neq 0$. This population difference is an odd function of the magnetic field B, and we will show in the following that it is directly proportional to the magnetization of the system. The energies of the phononic and electronic excitation branches can be obtained by solving $\mathrm{Det}(\mathbf{D}^{-1}(B\neq 0))=0$, which yields

$$\left(\omega^2-\Omega_{ph}^2\right)\left(\omega^2-\Omega_{el}^2\right)\pm 2\omega\left(\gamma B\left(\omega^2-\omega_0^2\right)+\tilde{g}^2\omega_0 f_{21}\right)+\gamma B\left(\gamma B\left(\omega^2-\omega_0^2\right)+2\tilde{g}^2\omega_0 f_{21}\right)=0. \tag{24}$$

For small magnetic fields, we can assume a solution of the form

$$w_{ph}^{\pm}=\Omega_{ph}(1\mp\eta) \tag{25}$$

and by substituting it in Eq. (24), we get

$$\Omega_{ph}\eta=\frac{\gamma B\left(\Omega_{ph}^2-\omega_0^2\right)+\tilde{g}^2\omega_0 f_{21}}{\Omega_{ph}^2-\Omega_{el}^2+\gamma^2B^2}. \tag{26}$$

Please see the Appendix for a detailed derivation. Consequentially, we obtain an expression for the splitting of the phonon frequencies,

$$\frac{\omega_{ph}^+-\omega_{ph}^-}{\Omega_{ph}}=2\frac{\gamma B\left(\Omega_{ph}^2-\omega_0^2\right)/\omega_0+\tilde{g}^2f_{21}}{\sqrt{\left(\omega_0^2-\Delta^2\right)^2+8\tilde{g}^2f_0\omega_0\Delta+\gamma^2B^2}}. \tag{27}$$

The complex hybridization of energy levels leading to this splitting is depicted in Fig. 2(b), and it arises from a combination of two factors: (1) a Zeeman shift of the electronic energy levels that is determined by the g factor of the Kramers states in each manifold, and (2) a population imbalance between the ground-state energy levels that is directly related to a change in spin polarization (and subsequently magnetization) of the ion.

The net spin polarization of the ground state of the system depends on magnetic field B, temperature T, and also on the exchange interactions in the system. We will derive an explicit form for the population asymmetry in Secs. III and IV, when considering the examples of paramagnets and magnets. For example, the population difference for the paramagnetic case is simply given by $f_{21}=\tanh\left(g_{gs}^{el}B/(k_BT)\right)$. On the other hand, for ferromagnetic or antiferromagnetic cases, its form is more complicated and can be derived by adding the exchange mean field. In all cases, in the limit $B\to 0$, we can write the

population difference as linear in the magnetic field,

$$f_{21} \approx \chi B, \tag{28}$$

where χ is directly related to the magnetic susceptibility of the system. As a result, for a small magnetic field, both the terms in Eq. (26) lead to Zeeman splitting of previously doubly degenerate phonon mode. We notice that the splitting becomes more pronounced as the noninteracting phonon energy ω_0 comes closer to electronic excitation energy Δ. Here, we can distinguish two different scenarios:

(1) *Resonant case:* $\Delta \approx \omega_0$ such that $|\omega_0 - \Delta| \ll \tilde{g}$. In this case, the relative splitting can be written as

$$\frac{\omega_{ph}^{+} - \omega_{ph}^{-}}{\Omega_{ph}} \approx \frac{\gamma + \frac{\tilde{g}}{\sqrt{2}}\chi}{\omega_0} B, \tag{29}$$

which depends linearly on the orbit-lattice coupling strength $\tilde{g}$.

(2) *Off-resonant case:* $|\omega_0 - \Delta| \gg \tilde{g}$. In this case, $\Omega_{ph}^2 - \omega_0^2 \approx \tilde{g}^2\omega_0/|\omega_0 - \Delta|$, and thus the relative splitting can be written as

$$\frac{\omega_{ph}^{+} - \omega_{ph}^{-}}{\Omega_{ph}(B=0)} \approx \tilde{g}^2 \frac{\frac{\gamma}{|\Delta-\omega_0|} + \chi}{(\omega_0 - \Delta)(\omega_0 + \Delta_0)} B, \tag{30}$$

which depends quadratically on $\tilde{g}$.

In this paper, only the second scenario will become relevant, where higher-order corrections to the self-energy matrix in Eq. (13) can be neglected. Generally, CEF transition frequencies and phonon frequencies are mismatched enough that the off-resonant scenario applies. In the off-resonant case, the splitting diminishes as the energy difference between phonon and electronic excitations increases, which requires ω_0 and Δ to be at least of similar order of magnitude to yield a significant effect.

So far, we discussed how the phonon energies are shifted but we have not investigated the consequences of the orbit-lattice coupling on the displacements associated with the eigenmodes. Assuming the off-resonant scenario, the phonon-displacement operators corresponding to the split phonon modes with frequencies ω_{ph}^{+} and ω_{ph}^{-} of the interacting Green's function matrix are given by

$$Q_{+} = \frac{1}{\sqrt{2}}(Q_a - iQ_b), \tag{31}$$

$$Q_{-} = \frac{1}{\sqrt{2}}(Q_a + iQ_b), \tag{32}$$

where $Q_a \sim (a + a^{\dagger})$ and $Q_b \sim (b + b^{\dagger})$ were the displacement operators corresponding to linearly polarized phonon modes a and b. This shows that the new modes, Q_{+} and Q_{-}, correspond to circular superpositions of the two orthogonal components and have opposite chiralities. We would like to emphasize at this point that these zone-centered phonon modes here become chiral as a result of time-reversal breaking. On the other hand, inversion symmetry breaking can allow chiral phonons at other high-symmetry points in the Brillouin zone, as studied in many two-dimensional hexagonal lattices [2,51].

The energies of the chiral phonons with opposite helicities split up in an external magnetic field, described by the general expression in Eq. (27). In the limit $B \to 0$, this splitting becomes linear in the magnetic field, which allows us to attribute an effective magnetic moment to the chiral phonons. We denote the effective magnetic moment of chiral phonons by μ_{ph}, and the splitting is accordingly given by

$$\omega_{ph}^{\pm} = \omega_0 \pm \mu_{ph} B. \tag{33}$$

The phonon magnetic moment can therefore be defined as

$$\mu_{ph} = \frac{1}{2} \frac{\partial(\omega_{ph}^{+} - \omega_{ph}^{-})}{\partial B}\bigg|_{B\to 0}. \tag{34}$$

The magnitude of phonon Zeeman splitting obtained here depends on the coupling between orbital excitations and phonons. In order to have strong coupling between electronic and phonon degrees of freedom, the energies of these excitations should be of the same order of magnitude as the phonon energies. In the following sections, we will apply this model to rare-earth trihalide paramagnets and transition-metal oxide magnets to predict the Zeeman splitting and effective magnetic moments of chiral phonons in these materials.

III. CHIRAL PHONONS IN 4*f* PARAMAGNETS

The splitting of optical phonons in paramagnetic rare-earth compounds was extensively studied in the 1970s in a series of experiments [40,41,48,52]. Amongst other compounds, it was shown that the rare-earth trihalide $CeCl_3$ exhibits a large splitting of doubly degenerate phonon modes in an external magnetic field. Recently, using the early experimental data on orbit-lattice coupling, it was predicted, in Ref. [26], that chiral phonons in this material can produce effective magnetic fields on the order of tens of tesla when coherently excited with ultrashort laser pulses. Subsequently, $CeCl_3$ has emerged as an interesting candidate to study magnetophononic and phonomagnetic properties of chiral phonons. We will determine the microscopic origin of the orbit-lattice coupling and apply the model derived in the previous section to predict the Zeeman splittings and effective magnetic moments in this material. We stress that this is a quantitative prediction using only microscopic parameters and *ab initio* results, without the need for phenomenological theory or experimental data.

A. Structural and electronic properties of $CeCl_3$

The rare-earth trihalide $CeCl_3$, shown in Fig. 4(a), crystallizes in the space group no. 176 (point group $6/m$) and its primitive unit cell contains eight atoms. The two Ce^{3+} ions are located at the $2c$ Wyckoff positions (shown as Ce_A^{3+} and Ce_B^{3+}) and the six Cl^{-} ions are located at the $6h$ Wyckoff positions (shown as Cl_{1A}^{-}, Cl_{2A}^{-}, Cl_{3A}^{-}, Cl_{1B}^{-}, Cl_{2B}^{-}, and Cl_{3B}^{-}). The eight-atom unit cell hosts 21 optical phonon modes consisting of the irreducible representations $2A_g + 1A_u + 2B_g + 2B_u + 1E_{1g} + 3E_{2g} + 2E_{1u} + 1E_{2u}$ [26]. Each Ce^{3+} ion has nine nearest neighbors arranged in three different planes as shown in Fig. 4(a) for the Ce^{3+} ion A.

The ground-state configuration of the Ce^{3+} ($4f^1$) ion is given by a nearly free-ion configuration of a $L = 3, S = 1/2$ state in accordance with Hund's rule. The spin-orbit coupling

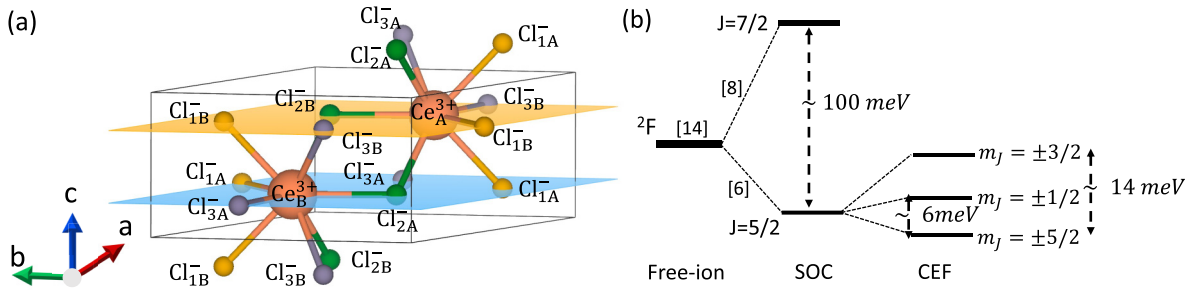

FIG. 4. Properties of $CeCl_3$. (a) Hexagonal crystal structure of $CeCl_3$ with point group $6/m$ and precise ionic labels. (b) Electronic energy levels of the Ce^{3+} ion. The energy levels compared to the free ion are split by spin-orbit coupling and by the crystal electric field, resulting in three Kramers doublets, of which $\pm 5/2$ is the ground state.

splits this 14-dimensional space into $J = 5/2$ and $J = 7/2$ total angular momentum sectors and the ground state is given by the six-dimensional $J = 5/2$ ($^2F_{5/2}$) state. Since there is only one electron in the $4f$ orbitals, the wavefunctions of different states in this multiplet can be written as

$$|J = 5/2, m_j = \pm 5/2\rangle = -\sqrt{\frac{1}{7}}\,|m_l = \pm 2, m_s = \pm 1/2\rangle + \sqrt{\frac{6}{7}}\,|m_l = \pm 3, m_s = \mp 1/2\rangle\,, \tag{35}$$

$$|J = 5/2, m_j = \pm 3/2\rangle = -\sqrt{\frac{2}{7}}\,|m_l = \pm 1, m_s = \pm 1/2\rangle + \sqrt{\frac{5}{7}}\,|m_l = \pm 2, m_s = \mp 1/2\rangle\,, \tag{36}$$

$$|J = 5/2, m_j = \pm 1/2\rangle = -\sqrt{\frac{3}{7}}\,|m_l = \pm 0, m_s = \pm 1/2\rangle + \sqrt{\frac{4}{7}}\,|m_l = \pm 1, m_s = \mp 1/2\rangle\,, \tag{37}$$

where $|m_l, m_s\rangle$ is a $4f$-orbital state with orbital quantum number m_l and spin quantum number m_s. The CEF further splits the states into three Kramers doublets $|\pm 5/2\rangle$, $|\pm 1/2\rangle$, and $|\pm 3/2\rangle$ with energies 0 meV, 5.82 meV, and 14.38 meV, respectively [41], as shown in Fig. 4(b).

B. Microscopic model for the orbit-lattice coupling

Previous Raman studies have shown that the doubly degenerate modes E_{1g} and E_{2g} split into left- and right-handed circularly polarized chiral phonon modes when a magnetic field is applied along the c axis of the crystal, perpendicular to the plane of the components of the doubly degenerate phonon modes [41,48]. In $CeCl_3$, the E_{1g} mode shows the largest splitting in experiment, and we will therefore first focus our analysis on this mode, which involves the displacement of Cl^- ions along the c axis. As there is only one E_{1g} phonon, the displacement pattern for this mode can be obtained directly from group theory and is given by

$$E_{1g}(a) = \frac{Q_a}{2\sqrt{6}}(0, 0, 2\hat{\mathbf{z}}, -\hat{\mathbf{z}}, -\hat{\mathbf{z}}, -2\hat{\mathbf{z}}, \hat{\mathbf{z}}, \hat{\mathbf{z}}), \tag{38}$$

$$E_{1g}(b) = \frac{Q_b}{2\sqrt{2}}(0, 0, 0, \hat{\mathbf{z}}, -\hat{\mathbf{z}}, 0, -\hat{\mathbf{z}}, \hat{\mathbf{z}}), \tag{39}$$

in the basis $(Ce_A^{3+}, Ce_B^{3+}, Cl_{1A}^-, Cl_{2A}^-, Cl_{3A}^-, Cl_{1B}^-, Cl_{2B}^-, Cl_{3B}^-)$ and $Q_{a/b}$ are the normal mode coordinates (amplitudes) of the two components a and b in units of $\text{Å}\sqrt{\text{amu}}$, where amu is the atomic mass unit. We show the atomic displacements corresponding to this mode in Fig. 5(a). The displacements of the Cl^- ions modify the Coulomb potential around the Ce^{3+} ions, which perturb the electronic Hamiltonian on the magnetic ion.

We use a point-charge model to describe the crystal electric field of the system, in which the potential energy of an electron at position $\mathbf{r}$ from Ce^{3+} nucleus, resulting from the nth Cl^- ion, is given by

$$V(\mathbf{R}_n, \mathbf{r}) = \frac{e^2}{4\pi\epsilon_0}\frac{1}{|\mathbf{R}_n - \mathbf{r}|}, \tag{40}$$

where $\mathbf{R}_n = \mathbf{R}_{0,n} + \mathbf{u}_n$ is the displacement of the nth ligand ion from Ce^{3+} nucleus, which depends on the equilibrium displacement $\mathbf{R}_{0,n}$ and the relative lattice displacement $\mathbf{u}_n$ arising from the phonon. The perturbation introduced by a given phonon mode can be obtained by a Taylor expansion of the potential in the lattice displacement $\mathbf{u}_n$ to linear order, which is done in Mathematica using the built-in series expansion function (see Appendix B for details). We express the displacements in terms of the normal coordinates $Q_{a,b}$ and sum over all nearest-neighbor ligands, which yields the first-order terms

$$V(E_{1g}(a)) = [-0.06xz + 0.16yz]Q_a\,\frac{\text{eV}}{\text{Å}^3\sqrt{\text{amu}}}, \tag{41}$$

$$V(E_{1g}(b)) = [0.16xz + 0.06yz]Q_b\,\frac{\text{eV}}{\text{Å}^3\sqrt{\text{amu}}}. \tag{42}$$

In spherical coordinates, $xz = r^2\cos\theta\sin\theta\cos\phi$ and $yz = r^2\cos\theta\sin\theta\sin\phi$, and we write the states from Eqs. (35)–(37) in terms of $4f$-basis states with the wave functions $\langle r|m_l, m_s\rangle = R(r)Y_3^{m_l}(\theta, \phi)$, where $R(r)$ is the radial part and $Y_3^{m_l}(\theta, \phi)$ is the spherical harmonic, see the

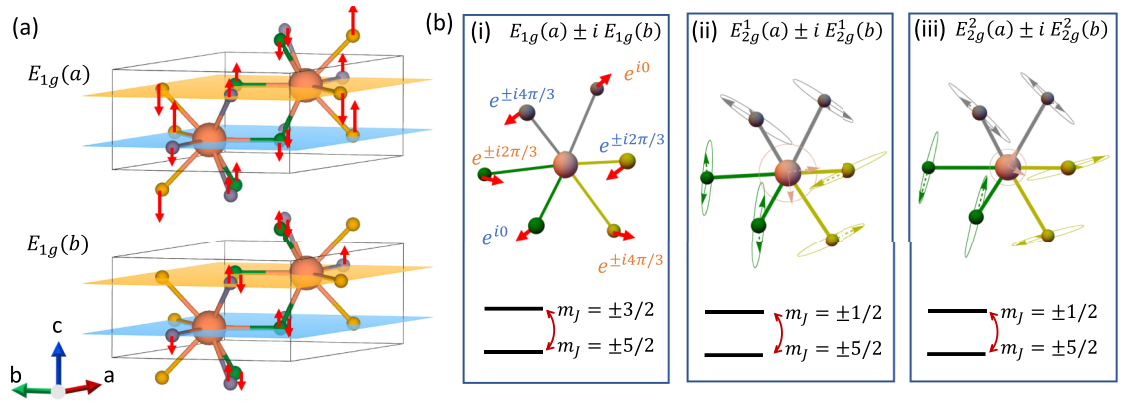

FIG. 5. Chiral phonons in $CeCl_3$. (a) Atomic displacements for the two components, a and b, of the doubly degenerate E_{1g} mode. Notably, both components involve only motion of the ions along the c direction of the crystal. (b) Displacement patterns for chiral phonons in the ab plane of the crystal arise from superpositions of the two components of the doubly degenerate E_{1g} and E_{2g} modes with a $\pi/2$ phase difference. We show the orbital transitions between the Kramers doublets that couple to the respective chiral phonon modes. (i) For E_{1g}, the Cl^- ions in the upper and lower plane around the Ce^{3+} ion move in opposite directions along the c-direction of the crystal with a relative phase of $\pm 2\pi/3$ between atoms lying in the same plane. [(ii),(iii)] For the E^1_{2g} and E^2_{2g} modes, all ions move on circular orbits around their equilibrium position in the ab plane of the crystal with different phase differences between different atoms.

Appendix for details. We evaluate the matrix elements of the above perturbations and obtain

$$H_1(xz) = -\frac{2}{7\sqrt{5}}\langle r^2\rangle \times \begin{pmatrix} & \left|\frac{5}{2},\pm\frac{5}{2}\right\rangle & \left|\frac{5}{2},\pm\frac{3}{2}\right\rangle \\ \left|\frac{5}{2}\pm\frac{5}{2}\right\rangle & 0 & \pm 1 \\ \left|\frac{5}{2},\pm\frac{3}{2}\right\rangle & \pm 1 & 0 \end{pmatrix}, \tag{43}$$

$$H_1(yz) = \frac{2}{7\sqrt{5}}\langle r^2\rangle \begin{pmatrix} & \left|\frac{5}{2},\pm\frac{5}{2}\right\rangle & \left|\frac{5}{2},\pm\frac{3}{2}\right\rangle \\ \left|\frac{5}{2},\pm\frac{5}{2}\right\rangle & 0 & i \\ \left|\frac{5}{2},\pm\frac{3}{2}\right\rangle & -i & 0 \end{pmatrix}, \tag{44}$$

where $\langle r^2\rangle = \int_0^\infty r^2 |R(r)|^2 r^2 dr$ is the mean-square $4f$-electron radius. We can write the phonon displacements as

$$Q_a = \frac{\hbar}{\sqrt{\hbar\omega_0}}(a + a^\dagger) = \frac{0.06\text{Å}\sqrt{\text{eV amu}}}{\sqrt{\hbar\omega_0}}(a + a^\dagger), \tag{45}$$

$$Q_b = \frac{\hbar}{\sqrt{\hbar\omega_0}}(b + b^\dagger) = \frac{0.06\text{Å}\sqrt{\text{eV amu}}}{\sqrt{\hbar\omega_0}}(b + b^\dagger), \tag{46}$$

where we restored $\hbar$ and $\hbar\omega_0$ is the energy of phonon mode.

The orbit-lattice coupling operators connecting the different electronic states in Eqs. (10) and (11) then become

$$\widehat{\mathbf{O}}_a = ge^{i\theta}\left|+\tfrac{5}{2}\right\rangle\left\langle+\tfrac{3}{2}\right| - ge^{-i\theta}\left|-\tfrac{5}{2}\right\rangle\left\langle-\tfrac{3}{2}\right| + \text{H.c.}, \tag{47}$$

$$\widehat{\mathbf{O}}_b = ige^{i\theta}\left|+\tfrac{5}{2}\right\rangle\left\langle+\tfrac{3}{2}\right| + ige^{-i\theta}\left|-\tfrac{5}{2}\right\rangle\left\langle-\tfrac{3}{2}\right| + \text{H.c.} \tag{48}$$

Here, we combined Eqs. (41)–(46) in order to obtain $g = -\sqrt{0.16^2 + 0.06^2}\frac{2}{7\sqrt{5}}\langle r^2\rangle\frac{0.06}{\sqrt{\omega_0}}\text{eV}^{3/2}/\text{Å}^2$ and $\tan(\theta) = 0.16/0.06$. From the general expression of the orbit-lattice coupling in Eqs. (10) and (11), we find that $g_a = ig_b = ge^{i\theta}$. Following our previously derived model, this orbit-lattice coupling leads to a splitting of the E_{1g} mode into two circularly polarized phonon modes with opposite chirality. The split modes have orbital angular momenta of $\pm\hbar$, arising from the superpositions $E_{1g}(a) \pm iE_{1g}(b)$ obtained from Eqs. (38) and (39). This can also be seen by applying a $C_3(z)$ rotation operation around each Ce^{3+} site, as the phonon mode is an eigenstate of the $C_3(z)$ operator with the eigenvalue $e^{i2\pi/3}$. The displacements associated with the opposite chiral phonon modes are depicted in the first panel of Fig. 5(b) alongside the orbital transitions with which they hybridize. The orbital angular momentum for these modes arises from the relative phase between neighboring atoms.

C. Phonon Zeeman splitting and effective phonon magnetic moment

We now proceed to computing the energy splitting and the effective phonon magnetic moments that can be associated with the chiral phonon modes. For the E_{1g} phonon mode, $\omega_0 = 22.75$ meV and $g = 7\,\text{meV/Å}^2\langle r^2\rangle$. With a mean-square radius of $\langle r^2\rangle \sim 0.1$ Å^2 [53], we get $g \sim 0.7$ meV. The splitting of the phonon modes is given by Eq. (27), where the relative contributions of the two additive terms depend on the values of the orbit-lattice coupling g, the energy difference between the electronic excitation and the phonon mode $\omega_0 - \Delta$, and the occupancy difference f_{21}. $CeCl_3$ is a paramagnetic system and the population difference for the two states in the ground-state Kramer doublet is given by

$$f_{21} = \tanh\left(\frac{5}{2}\frac{g^{el}_{5/2}\mu_B B}{k_B T}\right), \tag{49}$$

where $g^{el}_{5/2} \approx 4/5$ is the electronic g factor for the $J = 5/2$ states. In the regime $\mu_B B \ll k_B T$, we can approximate the population difference in linear order, $f_{21} \approx 2\mu_B B/k_B T$. We can safely assume the off-resonant scenario, as the electronic excitation energy of $\Delta \approx 16$ meV results in $|\omega_0 - \Delta| \gg \tilde{g}$. We accordingly can approximate Eq. (27) by Eq. (30),

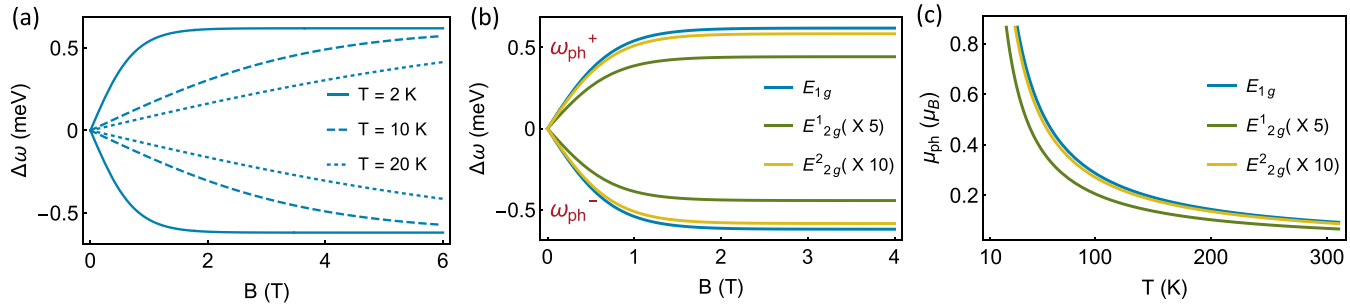

FIG. 6. Phonon Zeeman effect and effective phonon magnetic moments in $CeCl_3$. (a) Splitting of the doubly degenerate E_{1g} mode with frequency ω_0 into left- and right-handed circularly polarized chiral phonon modes with frequencies $\omega_{ph}^{\pm}$, as a function of the applied magnetic field, B. For strong magnetic fields, the magnetization and therefore the splitting saturates. The lower the temperature, the lower magnetic field strengths are required to reach saturation. (b) Phonon Zeeman splitting for the three different E_{ig} phonon modes of $CeCl_3$ at 2 K. (c) Effective phonon magnetic moments of the three different E_{ig} phonon modes, as a function of temperature.

yielding

$$\gamma B\left(\Omega_{ph}^2 - \omega_0^2\right) + \tilde{g}^2 f_{21}\omega_0 \approx \tilde{g}^2\omega_0\left(\frac{\gamma B}{\omega_0 - \Delta_0} + \frac{2\mu_B B}{k_B T}\right), \tag{50}$$

where $\gamma = (5/2 - 3/2)g_{5/2}^{el}\mu_B = 2/5\,\mu_B$. As a result, the relative contribution of the two terms in Eq. (50) depends on the temperature. In the present case for the E_{1g} mode, the second term dominates in the low-temperature regime, but the two contributions become equal when $k_B T \approx 5(\omega_0 - \Delta_0) = 50$ meV, that is at 500 K. We therefore only consider the contribution from the second term, which depends on the difference in occupation of two states in the ground-state Kramers doublet $|\pm 5/2\rangle$.

We show the phonon Zeeman splitting according to Eq. (50) in Fig. 6(a). We obtain a value of 1.24 meV (10 cm^{-1}) for the saturated phonon splitting, which is reasonably close to the value of 18 cm^{-1} observed in Ref. [41]. The relative splitting reaches more than 5% at saturation, and the magnitude of the magnetic fields required to reach saturation increases with temperature, according to the dependence of $\tanh(\chi B)$ on f_{21}. The value of the effective phonon magnetic moment μ_{ph} is inversely proportional to the temperature, as shown in Fig. 6(c), and our model predicts $\mu_{ph} = 2.9\,\mu_B$ at $T = 10$ K, several orders of magnitude higher than those produced by purely ionic circular charge currents [7,8,12,27]. The values of the saturation splitting and μ_{ph} at three different temperatures are presented in Table I, which range between 0.1 μ_B at room temperature and up to 9.3 μ_B at 2 K.

A similar analysis can be done for the E_{2g}^1 (12.1 meV) and E_{2g}^2 (21.5 meV) phonon modes, whose displacements are depicted in Fig. 5(b). Here, because of the existence of two phonon modes with the same symmetry, the displacements cannot be unambiguously determined from group theory, and we compute the phonon eigenvectors using density functional theory calculations as published in prior study [26]. Using the point-charge model, we calculate the orbit-lattice coupling for these phonons, please see the Appendix B for details. These phonons couple with orbital excitations between the states $|m_j = \pm 5/2\rangle$ and $|m_j = \pm 1/2\rangle$, as illustrated in Fig. 5(c), which leads to the phonon Zeeman splitting shown in Fig. 6(b).

Our model predicts effective phonon magnetic moments of $\mu_{ph} = 0.4\,\mu_B$ and $\mu_{ph} = 0.27\,\mu_B$ at $T = 10$ K and a saturation splitting of 0.18 meV (1.5 cm^{-1}) and 0.12 meV (1 cm^{-1}) for E_{2g}^1 and E_{2g}^2, respectively as shown in Table I. According to Ref. [41], the observed saturation splitting of the E_{2g}^1 mode is 0.87 meV (7 cm^{-1}), which is about four times the values obtained from our microscopic model. On the other hand, no splitting was observed for E_{2g}^2 mode in the same experiment. Here again, the observed phonon magnetic moment decreases with temperature as shown in Fig. 6(c). This disagreement could be attributed either to the crudeness of our point-charge model or to the resolution of this experiment, which is limited to 1 cm^{-1}.

IV. CHIRAL PHONONS IN 3*d* MAGNETS

In the previous section, we discussed the example of rare-earth trihalides, where the giant magnetic response of chiral phonons originates from the coupling of CEF-split electronic levels with doubly degenerate optical phonons. In this section, we show that chiral phonons in 3*d*-electron magnets with

TABLE I. Calculated saturation splitting, phonon Zeeman splitting in an applied magnetic field of $B = 1$ T, as well as effective phonon magnetic moments at liquid helium, liquid nitrogen, and room temperature, for the different doubly degenerate phonon modes in $CeCl_3$.

Phonon mode	Saturation splitting	Splitting (1 T, 10 K)	μ_{ph}(2 K)	μ_{ph}(77 K)	μ_{ph}(295 K)
E_{1g}(22.75 meV)	1.24 meV	0.32 meV	9.3 μ_B	0.37 μ_B	0.1 μ_B
E_{2g}^1(12.1 meV)	0.18 meV	0.05 meV	1.3 μ_B	0.05 μ_B	0.01 μ_B
E_{2g}^2(21.5 meV)	0.12 meV	0.02 meV	0.88 μ_B	0.03 μ_B	0.01 μ_B

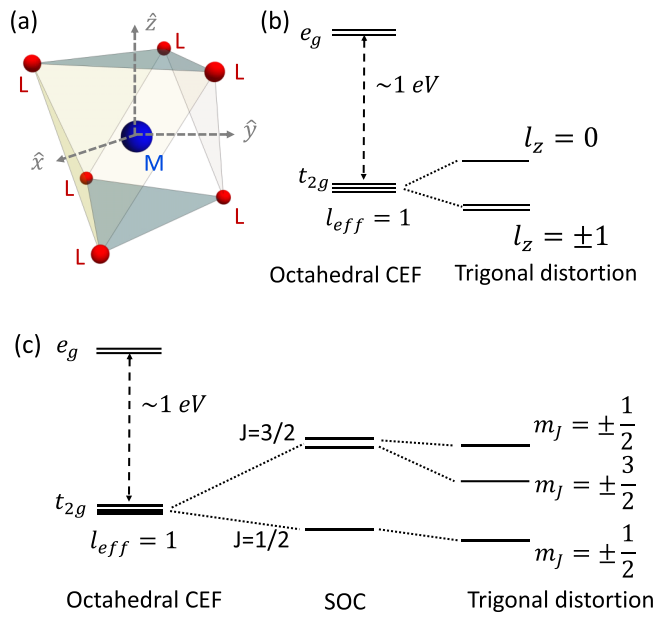

FIG. 7. Orbital configurations of d electrons in octahedral CEF. (a) A magnetic transition-metal ion M surrounded by a trigonally distorted octahedral cage of ligand ions L. The site symmetry of the magnetic ion is C_3. (b) The splitting of d orbitals resulting from a trigonal crystal field from the ligand arrangement on the left. (c) The splitting of d orbitals when spin-orbit coupling is stronger than the effect of the trigonal distortion.

octahedral ligand configuration can yield a similarly strong response. We begin with a general analysis of $3d$-orbital configurations and then perform calculations for the concrete example of $CoTiO_3$.

Materials with octahedral ligand configurations around the magnetic ion generally possess strong CEFs with splittings of the e_g and t_{2g} orbitals on the order of several eV. This renders the coupling between the $e_g - t_{2g}$ electronic excitations and phonons weak, and thus makes a magnetic response arising directly from these transitions unfeasible. In many materials, however, the t_{2g} and e_g manifolds are split further either by lattice distortions or spin-orbit coupling [54,55]. Both cases host electronic transitions with energies comparable to those of optical phonon modes, which leads to strong coupling and hybridization.

For the first case, consider a magnetic transition-metal ion surrounded by a trigonally distorted octahedron of ligand ions, as depicted in Fig. 7(a), as is commonly found in face-sharing octahedral geometries. Here, the site symmetry for a magnetic ion is reduced from O_h to C_3 and the t_{2g} manifold splits according to l_z, where the z axis is oriented along the C_3 rotation axis, as shown in Fig. 7(b). The energy of the states depends on the sign of the trigonal distortion, and the t_{2g} orbitals split into the two manifolds

$$|l_z = \pm 1\rangle = -\frac{1}{\sqrt{3}}(d_{xy} \mp i d_{x^2-y^2}) \pm \frac{i}{\sqrt{6}}(d_{xz} \mp i d_{yz}), \quad (51)$$

$$|l_z = 0\rangle = d_{3z^2-r^2}. \quad (52)$$

In the second case, the spin-orbit splitting is stronger than the splitting induced by the trigonal distortion, and we need to consider eigenstates characterized by the total angular momentum J as shown in Fig. 7(c). In this limit, the trigonal distortion introduces a perturbation of the form $H_{tri} = \delta J_z^2$ to the Hamiltonian of magnetic ion, which splits the $J = 3/2$ multiplet into two manifolds with $m_j \pm 1/2$ and $m_j = \pm 3/2$, while the $J = 1/2$ states remain unaffected.

In both scenarios, there are low-lying electronic transitions that involve a transfer of angular momentum of $\Delta m = \pm 1$, namely the transition from $|l_z = \pm 1\rangle$ to $|l_z = 0\rangle$ in the case of a trigonal distortion, and $|J = 1/2, m_j = \pm 1/2\rangle$ to $|J = 3/2, m_j = \pm 3/2\rangle$ in the case of spin-orbit coupling. These transitions are similar in nature to transitions from $|m_j = \pm 5/2\rangle$ to $|m_j = \pm 3/2\rangle$ in the example of the rare-earth trihalides in the previous section.

Next, let us consider an optical phonon mode that can be characterized by the E_g irreducible representation of the C_3 point group. There are many basis functions, corresponding to displacement patterns, that transform according to this irreducible representation for the system, shown in Fig. 7. One such possibility is the xy in-plane motion of a magnetic ion M located at the center of the trigonally distorted octahedra. The two components of the E_g mode are given by simple displacements of the ion M along the x and y directions, respectively, and result in the following form CEF perturbation,

$$V(E_g(a)) \propto xz\, Q_a \frac{\text{eV}}{\text{Å}^3\sqrt{\text{amu}}}, \quad (53)$$

$$V(E_g(b)) \propto yz\, Q_b \frac{\text{eV}}{\text{Å}^3\sqrt{\text{amu}}}, \quad (54)$$

where $Q_{a/b}$ are the normal mode coordinates associated with the two components $E_g(a/b)$, similar to Eqs. (41) and (42) in the case of the rare-earth trihalides discussed in the previous section. This perturbation results in a coupling similar to the one discussed in Eqs. (10) and (11) of Sec. II and can therefore lead to phonon chirality and a phonon Zeeman effect in a similar fashion.

The magnitude of this effect depends on the phonon energies, the electronic wave functions of states involved in the low-energy excitations, as well as their energies. As discussed in the previous section, the phonon magnetic moment can be significantly larger if the electronic excitation energy is closer to phonon energy. The typical energy scale associated with spin-orbit coupling and trigonal distortions is usually in the range 10–100 meV for d-electron systems, which puts these electronic excitations in close proximity with optical phonons and hence makes the above effect feasible. Additionally, most transition-metal systems have significant superexchange interactions with neighboring spins originating from the large spatial extent of the d orbitals. As a result, one should expect a rather different temperature trend for the phonon magnetic moment μ_{ph} below magnetic ordering temperatures, which can be evaluated by including the exchange mean-field contributions.

We next perform calculations for the concrete example of the XY-quantum magnet $CoTiO_3$, which is known to have spin-orbit excitations with energies comparable to a range of optical phonons in the system [56–59].

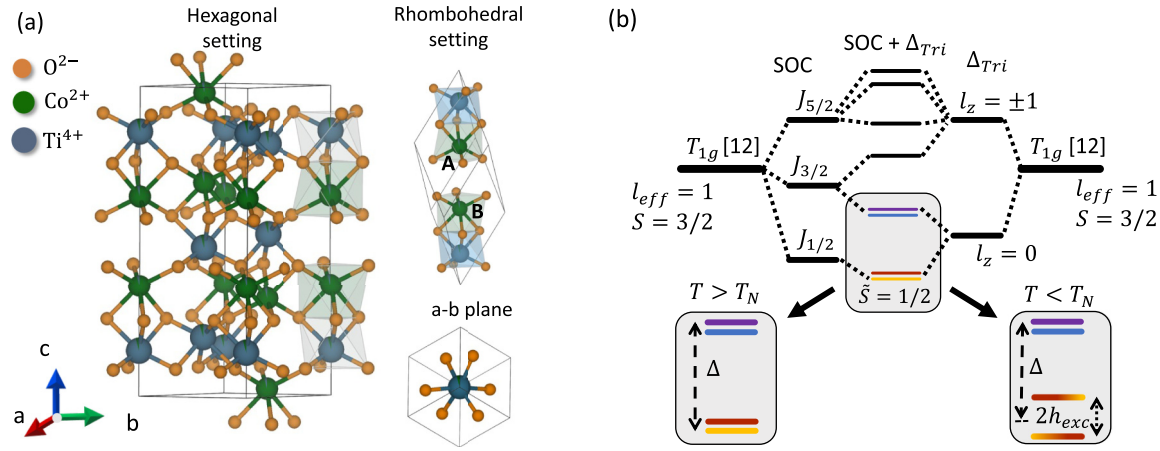

FIG. 8. Properties of $CoTiO_3$. (a) Crystal structure of transition-metal oxide $CoTiO_3$ in the ilmenite structure with trigonal space group $R\bar{3}$. Each of the Co^{2+} ions is surrounded by a trigonally distorted octahedral cage of O^{2-} ions. (b) Electronic energy levels of the Co^{2+} ion, which are split by a combination of the octahedral crystal field caused by the O^{2-} ions, the spin-orbit coupling, and the trigonal distortion of the octahedral cage. The low-energy manifold shown in the grey box contains two doublets separated by energy $\Delta = 23.5$ meV, which provide the spin-orbit excitation that can hybridize with the phonons. Below the Néel temperature, the ground-state manifold is further split by a temperature-dependent exchange mean-field $h_{\rm exc}$, which lies in $a-b$ plane.

A. Structural and electronic properties of $CoTiO_3$

The transition-metal oxide $CoTiO_3$ crystallizes in an ilmenite structure with the trigonal space group $R\bar{3}$ (point group 3). Each of the Co^{2+} ions is surrounded by a trigonally distorted octahedral cage of O^{2-} ions, as shown in Fig. 8(a). The rhombohedral unit cell contains two Co^{2+} ions, which we denote by A and B. The Co^{2+} ions are arranged in slightly buckled two-dimensional honeycomb lattices, which are stacked in an ABC sequence along the c axis of the crystal, with neighboring planes displaced diagonally by one-third of the unit cell. Below the Néel temperature of $T_N = 38$ K, the magnetic moments order ferromagnetically within the ab planes and are coupled antiferromagnetically along the c axis [56–58]. The rhombohedral unit cell contains 10 ions, and group theory predicts ten Raman-active phonons, $\Gamma_R = 5A_g \oplus 5E_g$, and eight infrared-active modes, $\Gamma_{IR} = 4A_u \oplus 4E_u$, where A and E denote nondegenerate and doubly degenerate modes, respectively [59,60].

The magnetic properties of $CoTiO_3$ are determined by the three unpaired spins on the magnetic Co^{2+} ion with $3d^7$ valence configuration. The spin-orbit coupling and trigonal distortion have the same energy scale in $CoTiO_3$ [56], and the ground state of Co^{2+}, $S = 3/2$, can be described as an effective $\tilde{S} = 1/2$ spin state, as shown in Fig. 8(b). The two low-energy manifolds are predominantly composed of $j_{\rm eff} = 1/2$ and $j_{\rm eff} = 3/2$ angular momentum states, respectively, and their wavefunctions are given by

$$\begin{aligned}|\psi_{1/2}\rangle &= \left|J=\frac{1}{2}, m_j = \pm\frac{1}{2}\right\rangle \\ &= \frac{1}{\sqrt{2}}\left|m_l = \mp\tilde{1}, m_s = \pm\frac{3}{2}\right\rangle \\ &\quad - \frac{1}{\sqrt{3}}\left|m_l = \tilde{0}, m_s = \pm\frac{1}{2}\right\rangle \\ &\quad + \frac{1}{\sqrt{6}}\left|m_l = \pm\tilde{1}, m_s = \mp\frac{1}{2}\right\rangle \end{aligned} \tag{55}$$

and

$$\begin{aligned}|\psi_{3/4}\rangle &= \left|J=\frac{3}{2}, m_j = \pm\frac{3}{2}\right\rangle \\ &= \sqrt{\frac{3}{5}}\left|m_l = \tilde{0}, m_s = \pm\frac{3}{2}\right\rangle \\ &\quad - \sqrt{\frac{2}{5}}\left|m_l = \pm\tilde{1}, m_s = \pm\frac{1}{2}\right\rangle, \end{aligned} \tag{56}$$

where the states $|m_l = \tilde{i}, m_s\rangle$ arise from the effective $l_{\rm eff} = 1$ and $S = 3/2$ states that are comprised of three holes. m_l and m_s denote the magnetic quantum numbers along the z-direction of the local coordinate system of the two Co^{2+} ions. Check Fig. 11 in the Appendix B for details.

For $T > T_N$, both manifolds remain doubly degenerate and the two manifolds are separated in energy by 23.5 meV [56], as measured in neutron-diffraction experiments. In the magnetically ordered phase at $T < T_N$, the ground-state manifold is split by the exchange mean-field resulting from the in-plane magnetic ordering of the spins. The low-energy excitations between these spin-orbit split states are very close in energy with two optical phonons with E_g symmetry at 26 meV and 33 meV [59]. This close proximity in energy enables the hybridization between phonons and spin-orbit excitations, which in turn can produce phonon chirality and therefore a phonon Zeeman effect.

B. Microscopic model for the orbit-lattice coupling

Phonons associated with irreducible representations other than fully symmetric ones lower the site symmetry of the Co^{2+} and hence can mix different electronic states. Here, we consider the two E_g modes with energies of 26 meV and 33 meV that are close to the orbital transitions. As in Sec. III, we first evaluate the strength of the coupling using a point-charge model with atomic displacements of phonons obtained from group theory and first-principles calculations.

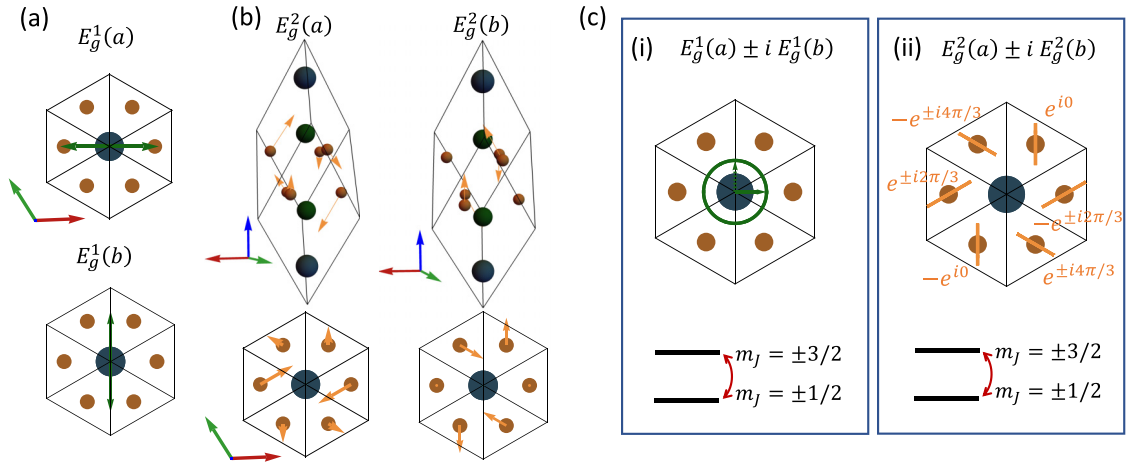

FIG. 9. Chiral phonons in $CoTiO_3$. (a) Atomic displacements for the two components, a and b, of the doubly degenerate E_g^1 mode. This mode involves only the motion of the Co^{2+} ion in the ab plane in two perpendicular directions. (b) Side and top view of atomic displacements for the two components, a and b, of the doubly degenerate E_g^2 mode. (c) Displacement patterns for chiral phonons in the ab plane of the crystal arise from superpositions of the two components of the doubly degenerate E_g^1 and E_g^2 modes with a $\pi/2$ phase difference. We further show the orbital transitions between the Kramers doublets that couple to the respective chiral phonon modes. (i) For the E_g^1 mode, the Co^{2+} ions move on circular orbits around their equilibrium position in the ab plane of the crystal. (ii) For the E_g^2 modes, the O^{2-} ions in the upper and lower plane around the Co^{2+} ions move in opposite directions, with a relative phase of $\pm 2\pi/3$ between atoms lying in the same plane.

We first find the basis functions for different phonon modes by using projection operators for the irreducible representation E_g. The phonon displacements of two E_g modes under consideration are a superposition of these basis functions and cannot be obtained from purely group theoretical tools. However, first-principal calculations in previous works [59] allowed us to approximate the lattice displacements in terms of the basis functions. The E_g^1 (26 meV) mode is predominantly associated with the motion of the Co^{2+} ion in the ab plane, which, in the basis function of the two components of the E_g^1 mode, can be approximated as x and y motion of the Co^{2+} ion, as shown in Fig. 9(a), where $\hat{\mathbf{x}}$ and $\hat{\mathbf{y}}$ are two orthonormal vectors in the a-b plane. We are using the local coordinate system shown in Fig. 11 of Appendix B.

For the E_g^2 (33 meV) mode, we used a superposition of basis functions that matches the displacements, shown in Fig. 9(b), to the E_g^2 mode in previous first-principles calculations in Ref. [59]. For the E_g^2 mode, we tried several superpositions of different basis functions and have considered the one that showed displacements, as in Fig. 9(b), similar to the E_g^2 mode in the first-principles calculations in Ref. [59]. The E_g^2 mode primarily includes the motion of ligand O^{2-} ions. For the displacements shown in Fig. 9(c), we find that the modifications of the CEF around the A- and B-site Co^{2+} ions for the E_g^1 mode are given by

$$V^{A/B}\big(E_g^1(a)\big) = [-0.56\,\mathrm{eV}xz - 0.51\,\mathrm{eV}(x^2-y^2) + \mathcal{O}(r^3)]Q_a, \tag{57}$$

$$V^{A/B}\big(E_g^1(b)\big) = \pm[1.0\,\mathrm{eV}xy - 0.56\,\mathrm{eV}yz + \mathcal{O}(r^3)]Q_b. \tag{58}$$

For the E_g^2 modes, they are given by

$$V^{A/B}\big(E_g^2(a)\big) = [-0.04\,\mathrm{eV}xy - 0.61\,\mathrm{eV}xz]Q_a + [0.72\,\mathrm{eV}yz - 0.14\,\mathrm{eV}(x^2-y^2) + \mathcal{O}(r^3)]Q_a \tag{59}$$

$$V^{A/B}\big(E_g^2(b)\big) = \pm[0.28\,\mathrm{eV}xy - 0.72\,\mathrm{eV}xz - 0.61\,\mathrm{eV}yz]Q_b \pm [-0.02\,\mathrm{eV}(x^2-y^2) + \mathcal{O}(r^3)]Q_b, \tag{60}$$

where $Q_{a/b}$ again denote the normal mode coordinates associated with the two components of the E_g phonon modes in a local coordinate system around each Co^{2+} ion, given in units of $\text{Å}\sqrt{\text{amu}}$. The z and x axis for B sites are opposite to that of A sites (see Fig. 11 in Appendix B for more details), which explains an extra negative sign in the b component correction for B sites in Eq. (60). In the basis of $|\psi_{1/2}\rangle = |J = 1/2, m_j = \pm 1/2\rangle$ and $|\psi_{3/4}\rangle = |J = 3/2, m_j = \pm 3/2\rangle$, the resulting coupling, shown also shown in Fig. 9(c), takes the following form for the two components of E_g mode modes:

$$\hat{\mathbf{O}}^{A/B}_{E_g^a} = g e^{i\phi_{ab}} \left|\psi_1^A\right\rangle\left\langle\psi_3^A\right| - g e^{-i\phi_{ab}} \left|\psi_2^A\right\rangle\left\langle\psi_4^A\right| + \text{H.c.}, \tag{61}$$

$$\hat{\mathbf{O}}^{A/B}_{E_g^b} = \pm i g e^{i\phi_{ab}} \left|\psi_1^A\right\rangle\left\langle\psi_3^A\right| \pm i g e^{-i\phi_{ab}} \left|\psi_2^A\right\rangle\left\langle\psi_4^A\right| + \text{H.c.}. \tag{62}$$

The coupling factors g for the two E_g modes are given by

$$g_{E_g^{(1)}} \approx 0.3 r_0^2/\text{Å}^2\text{meV} \quad \text{and} \quad g_{E_g^{(2)}} \approx 0.4 r_0^2/\text{Å}^2\text{meV}, \tag{63}$$

where $r_0^2 = \langle r^2\rangle \approx 1\,\text{Å}^2$ for $3d$ orbitals in Co^{2+} [61] (see Appendix C). The phase ϕ_{ab} depends on the ratio of the coefficients of the $xz(xy)$ and $yz(x^2-y^2)$ terms, but does not affect the self-energy terms.

To compute the coupling strength g, we first express the phonon displacements in terms of the phononic creation and annihilation operators, a, $a^\dagger$, b, and $b^\dagger$, analogously to

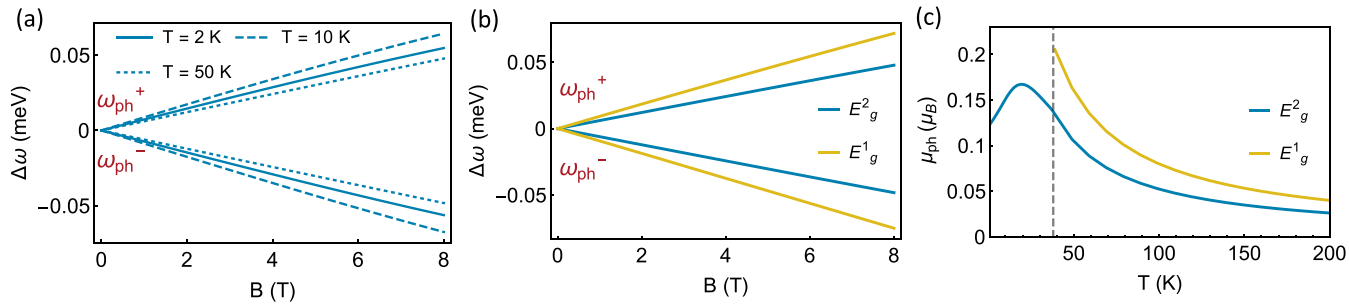

FIG. 10. Phonon Zeeman effect and effective phonon magnetic moments in $CoTiO_3$. (a) Splitting of the doubly degenerate E_g^2 mode with frequency ω_0 into left- and right-handed circularly polarized phonon modes with frequencies $\omega_{ph}^{\pm}$, as a function of the applied magnetic field B along c axis at three different temperatures. (b) Phonon Zeeman splitting for E_g^1 and E_g^2 mode at 50 K. (c) Phonon magnetic moment, μ_{ph}, as a function of temperature for E_g^1 and E_g^2 mode. The phonon magnetic moment increases with decreasing temperature in the paramagnetic regime. The E_g^2 mode shows very distinct behavior below and above Néel temperature, $T_N = 38$ K shown by the dotted line. The E_g^1 mode is very close in energy to the spin-orbit excitation and both energies are affected by the magnetic transition, which would significantly influence the hybridization mechanism and is not captured in our model.

Eqs. (45) and (46),

$$Q_a = \frac{\hbar}{\sqrt{\hbar\omega_0}}(a + a^\dagger) = \frac{0.06\text{Å}\sqrt{\text{eV amu}}}{\sqrt{\hbar\omega_0}}(a + a^\dagger). \quad (64)$$

$$Q_b = \frac{\hbar}{\sqrt{\hbar\omega_0}}(b + b^\dagger) = \frac{0.06\text{Å}\sqrt{\text{eV amu}}}{\sqrt{\hbar\omega_0}}(b + b^\dagger). \quad (65)$$

where we restored $\hbar$ and $\hbar\omega_0$ is the phonon energy. Using Eqs. (57)–(60) and expressing the states in Eqs. (55) and (56) in terms of three-particle d-orbital states, we evaluate the matrix elements for the CEF perturbation term between different states (see the Appendix for details). This coupling term maps to Eqs. (10) and (11) in Sec. II, and, accordingly, the E_g modes will split into circularly polarized modes with opposite chirality when a magnetic field is applied along the c axis. The split modes will have angular momenta of $\pm\hbar$ along the c axis, which arises from the orbital angular momentum possessed by the superpositions $E_g(a) \pm iE_g(b)$ shown in Fig. 9(c).

C. Phonon Zeeman splitting and effective phonon magnetic moment

In order to evaluate the phonon Zeeman splitting for both of these E_g modes, we can apply the model discussed in Sec. II with slight modifications. For $T > T_N$, the system is in the paramagnetic phase and the eigenstates of the two manifolds involved in electronic excitations are identical to $|\psi_{1/2}\rangle$ and $|\psi_{3/4}\rangle$ as described by Eqs. (55) and (56), respectively. In this case, after accounting for the orbit-lattice interaction described by Eqs. (61) and (62), the phonon Green's function can be written as

$$\mathbf{D}^{-1}(\omega) = \begin{pmatrix} \frac{\omega^2-\omega_0^2}{2\omega_0} - \tilde{g}^2\left(\frac{f_1^A\Delta_1^A}{\omega^2-(\Delta_1^A)^2} + \frac{f_2^A\Delta_2^A}{\omega^2-(\Delta_2^A)2} + A \Longleftrightarrow B\right) & i\tilde{g}^2\left(-\frac{f_1^A\omega}{\omega^2-(\Delta_1^A)^2} + \frac{f_2^A\omega}{\omega^2-(\Delta_2^A)^2} - A \Longleftrightarrow B\right) \\ -i\tilde{g}^2\left(-\frac{f_1^A\omega}{\omega^2-(\Delta_1^A)^2} + \frac{f_2^A\omega}{\omega^2-(\Delta_2^A)^2} - A \Longleftrightarrow B\right) & \frac{\omega^2-\omega_0^2}{2\omega_0} - \tilde{g}^2\left(\frac{f_1^A\Delta_1^A}{\omega^2-(\Delta_1^A)^2} + \frac{f_2^A\Delta_2^A}{\omega^2-(\Delta_2^A)^2} + A \Longleftrightarrow B\right) \end{pmatrix}, \quad (66)$$

where again $\tilde{g}^2 = 4\pi g^2$.

The correction to the noninteracting phonon Green's function here is similar to that in Eq. (20) discussed in Sec. II. The only difference is that the off-diagonal term has contributions from two magnetic ions denoted by A and B. The contributions from the two ions come with opposite signs, but it is also worth noticing that the orbit-lattice coupling were evaluated within the local coordinate systems of each of the ions. The local z coordinates for the two ions point in opposite directions and thus, for a magnetic field applied along the c axis of the crystal, the population difference for two states in the lower Kramers doublet ($J = 1/2$) are opposite as well, which means that the two contributions add up.

Following the same procedure as in Sec. II and Sec. III, we obtain the phonon Zeeman splitting shown in Fig. 10(a). We have used the values of orbit-lattice coupling from Eq. (63), $\Delta_1 = \Delta_2 = 23.5$ meV, a magnetic moment of $\mu_{el}^{gd} = 1.9\,\mu_B$ for the $J = 1/2$ ground-state manifold of Co^{2+} on the basis of the range mentioned in Ref. [56], as well as $\omega_{ph} = 26$ meV and $\omega_{ph} = 33$ meV for the E_g^1 and E_g^2 modes, respectively. At a temperature of $T = 50$ K, this leads to significant splitting for both modes, as shown in Fig. 10(b), yielding phonon magnetic moments of $\mu_{ph} = 0.2\,\mu_B$ and $0.1\,\mu_B$ for E_g^1 and E_g^2, respectively. In the paramagnetic regime, we expect the temperature dependence of μ_{ph} to be $1/T$, according to Eq. (50), and hence decreases monotonously with increasing T, as shown in Fig. 10(c). The phonon magnetic moment reduces to $0.07\,\mu_B$ ($0.05\,\mu_B$) for $E_g^1(E_g^2)$ phonon at room temperature as shown in Table II.

However, this analysis does not work below the Neel temperature. For $T < T_N$, the spins order antiferromagnetically and develop a finite in-plane magnetic moment. The exchange

TABLE II. Calculated saturation splitting, phonon Zeeman splitting in an applied magnetic field of $B = 1$ T at 10 K, as well as effective phonon magnetic moments at liquid helium, two different temperatures below and above the Neél temperature, and room temperature, for doubly degenerate E_g^2 phonon mode in $CoTiO_3$. The E_g^1 mode does not exist in the same form below the Neél temperature, and accordingly provide values for temperatures above it. The phonon Zeeman splitting of both phonon modes does not saturate for the field strengths investigated here.

Phonon mode	Saturation splitting	Zeeman splitting (1 T, 10 K)	μ_{ph}(2 K)	μ_{ph}(40 K)	μ_{ph}(77 K)
E_g^1(33 meV)	>0.1 meV			0.2 μ_B	0.07 μ_B
E_g^2(33 meV)	>0.1 meV	0.02 meV	0.13 μ_B	0.14 μ_B	0.04 μ_B

field arising from the spin ordering alters the single-ion energy levels and their eigenstates. Without loss of generality, we can assume that the resulting exchange mean-field points along the x direction, which splits up the lower ground-state Kramers doublet even in the absence of the external magnetic field, as illustrated in Fig. 8(b). The upper manifold is not affected, but new eigenstates are formed for the lower manifold that are given by

$$\begin{pmatrix} \mu_{el}^{gd} B_z^{\alpha} & h_{ex}(T) \\ h_{ex}(T) & -\mu_{el}^{gd} B_z^{\alpha} \end{pmatrix} \left|\psi_{\tilde{1}/\tilde{2}}^{\alpha}\right\rangle = E_{\tilde{1}/\tilde{2}} \left|\psi_{\tilde{1}/\tilde{2}}^{\alpha}\right\rangle \tag{67}$$

where the Hamiltonian is written in the basis $(|\psi_1^{\alpha}\rangle, |\psi_2^{\alpha}\rangle)$ defined in Eq. (55). The index $\alpha = A, B$ denotes the Co^{2+} ion site, $h_{ex}(T)$ is the exchange mean field, and B_z is the external magnetic field. The energy difference is given by $E_{\tilde{2}} = -E_{\tilde{1}} = \sqrt{(\mu_{el}^{gd} B_z)^2 + h_{ex}^2(T)}$.

We can now apply our orbit-lattice coupling model for these new eigenstates and obtain the phonon energies by solving $\mathrm{Det}(\mathbf{D}^{-1}(\omega)) = 0$. The diagonal components are given by

$$\begin{aligned} \mathbf{D}^{-1}|_{aa} &= \mathbf{D}^{-1}|_{bb} \\ &= \frac{\omega^2 - \omega_0^2}{2\omega_0} - 2\tilde{g}^2 \left(\frac{f_{\tilde{1}} E_{\tilde{1}3} \left(\cos\frac{\theta}{2}\right)^2}{\omega^2 - E_{\tilde{1}3}^2} + \frac{f_{\tilde{1}} E_{\tilde{1}4} \left(\sin\frac{\theta}{2}\right)^2}{\omega^2 - E_{\tilde{1}4}^2} \right) \\ &\quad - 2\tilde{g}^2 \left(\frac{f_{\tilde{2}} E_{\tilde{2}3} \left(\sin\frac{\theta}{2}\right)^2}{\omega^2 - E_{\tilde{2}3}^2} + \frac{f_1 E_{24} \left(\cos\frac{\theta}{2}\right)^2}{\omega^2 - E_{\tilde{2}4}^2} \right), \end{aligned} \tag{68}$$

and the off-diagonal components in turn are given by

$$\begin{aligned} \mathbf{D}^{-1}|_{ab} &= -\mathbf{D}^{-1}|_{ba} \\ &= 2i\tilde{g}^2 \left(-\frac{f_{\tilde{1}} \omega \left(\cos\frac{\theta}{2}\right)^2}{\omega^2 - E_{\tilde{1}3}^2} + \frac{f_{\tilde{1}} \omega \left(\sin\frac{\theta}{2}\right)^2}{\omega^2 - E_{\tilde{1}4}^2} \right) \\ &\quad + 2i\tilde{g}^2 \left(-\frac{f_{\tilde{2}} \omega \left(\sin\frac{\theta}{2}\right)^2}{\omega^2 - E_{\tilde{2}3}^2} + \frac{f_{\tilde{2}} \omega \left(\cos\frac{\theta}{2}\right)^2}{\omega^2 - E_{\tilde{2}4}^2} \right), \end{aligned} \tag{69}$$

where $\cos(\theta) = \mu_{el}^{gd} B \sqrt{(\mu_{el}^{gd} B)^2 + h_{ex}^2(T)}$, $E_{\tilde{1}3} = E_{\tilde{1}4} = \Delta_0 - E_{\tilde{1}}$, $E_{\tilde{2}3} = E_{\tilde{2}4} = \Delta_0 - E_{\tilde{2}}$, and where $h_{ex}(T) = h_0\sqrt{(1 - T/T_N)}$ is the temperature-dependent exchange mean field.

Here, the structure of the eigenstates $(|\psi_{\tilde{1}}\rangle, |\psi_{\tilde{2}}\rangle)$ is such that the off-diagonal terms come out to be zero when the states are an equal superposition of $|\psi_1\rangle$ and $|\psi_2\rangle$, which is the case for $B = 0$, where no phonon energy splitting occurs as expected. However, once a magnetic field is applied along the c axis of the crystal, the eigenstates in the ground-state manifold are no longer an equal superposition of up and down spins and develop a net magnetic moment along the c direction. As a result, the off-diagonal terms become proportional to B, leading to a splitting of the previously degenerate phonon modes as shown in Figs. 10(a) and 10(b). Interestingly, the splitting does not saturate even at very low temperatures, which can be understood on the basis of exchange interactions.

For temperatures below T_N, the temperature dependence therefore enters in two different ways: First, it determines the thermal population of the two states in the ground-state manifold, and second, it determines the spin polarization of each state through the temperature-dependence of the exchange mean field. This combination makes the problem analytically untractable, and hence we obtain the phonon frequencies by numerically evaluating the poles of Green's functions. We show the combined temperature dependence of μ_{ph} above and below the Néel temperature in Fig. 10(c), where we have considered a maximum exchange mean field of $h_0 = 3$ meV on the basis of the values presented in Ref. [56]. We find the phonon magnetic moment $\mu_{ph} = 0.13\,\mu_B$ at liquid helium temperature, which is comparable to the value obtained at 40 K, $T \approx T_N$ as shown in Table II.

In both cases, $T > T_N$ and $T < T_N$, the phonon splitting is nonzero only if the populations and eigenstates of the ground-state manifold are such that the magnetic ion carries a net magnetic moment along the c axis. In the paramagnetic case, the magnetic moment is directly related to the population difference of the two states in the lower Kramers doublet, as the two states have a magnetic moment along the c axis, but with opposite signs. In contrast, in the antiferromagnetically ordered state, we further need to take into account the net magnetic moment of each state in addition to the population difference between the two states. The direction of the net magnetic moment of each state is therefore determined by the combined effect of the in-plane exchange mean field and out-of-plane applied magnetic field. As a result, the net magnetization of the sample increases at a slower rate with the applied magnetic field in the $T < T_N$ case, compared to the paramagnetic region. This rate keeps on decreasing as the temperature is decreased further and leads to a maximum of the phonon magnetic moment below the Néel temperature, in contrast to the divergence in the pure paramagnetic case of the rare-earth trihalides. Overall, we can expect that the temperature trend of the phonon magnetic moment should be similar to the temperature dependence of the magnetic susceptibility along the c direction.

Our calculations for $CoTiO_3$ have shown two things: (1) applying an external magnetic field can produce chiral phonons with large effective magnetic moments on the order

of $0.1\,\mu_B$, and (2) the phonon magnetic moment follows the same trend as the magnetic susceptibility. This intuition can be extended to ferromagnets, where we expect that the phonon Zeeman splitting would saturate very quickly near the critical temperature and chiral phonons would remain split with fixed energy separation below T_C. It also indicates that in some cases, it is possible to have chirality-dependent phonon energy splitting even in the absence of an external magnetic field [62].

V. DISCUSSION

In summary, we have developed a microscopic model that describes the hybridization of doubly degenerate phonon modes with electronic orbital transitions between doublet states. An applied magnetic field splits the degeneracy of the doublets and therefore that of the phonons coupled to it, resulting in circularly polarized phonon modes with opposite chirality. The splitting is determined by the population asymmetry between the ground-state doublets, which makes the mechanism temperature dependent. The splitting of the phonon frequencies is linear in the limit of small magnetic fields, which is consistent with the phenomenological notion of the phonon Zeeman effect [7,8], and allows us to assign an effective magnetic moment to the chiral phonon modes. The specific form of the orbit-lattice coupling leading to these phenomena depends on the point-group symmetry and orbital configuration of the material. Furthermore, in order for the mechanism to be significant, the phonon modes and orbital transitions need to be on similar energy scales. We have therefore applied the model and computed phonon Zeeman splittings and effective phonon magnetic moments for the specific cases of $CeCl_3$, a $4f$-electron paramagnet, in which the orbital transition between the doublet states are determined by the crystal electric field, as well as $CoTiO_3$, a $3d$-electron antiferromagnet, in which the orbital transitions are determined by spin-orbit coupling and a trigonal distortion.

In the case of $CeCl_3$, the effective phonon magnetic moment increases monotonically with decreasing temperature over the entire investigated temperature spectrum, because the spins of the Ce^{3+} ions order only at very low temperatures of <0.1 K [63], not considered here. We predict values of several μ_B at cryogenic temperatures that correspond to phonon frequency splittings of the order of 10 cm^{-1}, corroborating early experimental measurements [40,41]. Even at room temperature, the effective magnetic moments of the phonon modes range between $0.01\,\mu_B$ and $0.1\,\mu_B$, orders of magnitude larger than those generated by purely ionic charge currents [7,8,12,27,38,39]. In the case of $CoTiO_3$, we distinguish between the high-temperature paramagnetic and the low-temperature antiferromagnetic phases. The paramagnetic phase behaves similar to the case of $CeCl_3$, with a monotonically increasing effective phonon magnetic moment for decreasing temperatures down to the Néel temperature. Below the Néel temperature, however, the value of the magnetic moment peaks at approximately $0.17\,\mu_B$, because the exchange mean field in the ordered state exhibits an additional, competing temperature dependence that produces a global maximum of the effective magnetic moment of the phonon. Despite the decreasing trend of the magnetic moment at high temperatures, even at room temperature, we still obtain $\mu_{ph} = 0.07\,\mu_B$. Combining both temperature dependencies below and above T_N, the effective phonon magnetic moment follows roughly the trend of the magnetic susceptibility.

While we have looked at two particular examples in this paper, the theory developed in Sec. II is general to all materials that exhibit doubly degenerate phonon modes and orbital transitions between doublet states with comparable energy scales. We therefore expect that in particular more $3d$ transition-metal oxide compounds may show the proposed phenomena, which host a variety of materials with trigonal point-group symmetries and octahedral coordinations of ligand ions. Beyond transition-metal oxides, $4d$-electron magnets could be interesting candidates, because they possess larger spin-orbit couplings and therefore higher transition energies between doublet states, which allows hybridizations with high-frequency phonon modes above 10 THz (40 meV). $RuCl_3$, for example, possesses orbital excitations on the order of 100 meV [64] as well as doubly degenerate phonon modes with energies around 50 meV.

In magnetically ordered materials, the details of the mechanism for phonon Zeeman splitting further depend on the exchange interactions between the magnetic ions, and an upcoming challenge will be to investigate how the phenomenon unfolds when interactions such as superexchange, itinerant electrons, or ring-exchange interactions [65,66] are present. Beyond CEF and spin-orbit excitations, the mechanism can be extended to include hybridizations between doubly degenerate phonon modes and other electronic or collective excitations, such as low-energy charge-transfer excitations or magnons, which show strong magnetic-field dependence [67–70].

We point out that we have investigated only Raman-active phonon modes with $E_{(i)g}$ symmetries in this study. The same evaluation can be done for infrared-active phonon modes, $E_{(i)u}$ symmetries in our investigated materials, which can be resonantly driven with ultrashort laser pulses in the terahertz and mid-infrared spectral range [7,30]. A recent study proposed that infrared-active phonon modes driven in paramagnetic $CeCl_3$ can potentially produce giant effective magnetic fields through the effective magnetic moment of the phonons [26], and this phenomenon was subsequently experimentally demonstrated in a paramagnetic oxide/ferrimagnetic garnet heterostructure [31] and in CeF_3 [32]. In $CoTiO_3$, this mechanism should be readily applicable to the infrared-active E_u^1 and E_u^2 modes that can be driven with mid-infrared light. Coherent chiral phonon driving combined with large effective phonon magnetic moments provides a route towards generating nonequilibrium spin configurations [71] and towards unprecedented spin-switching protocols that could establish a new paradigm in ultrafast spintronics and data processing.

Finally, a note on the chirality of the phonons: Circularly polarized phonons directly at the Gamma point are generally achiral in 3D. Because they carry an angular momentum, represented by an axial vector, they could hence be considered axial phonons. In most cases, the phonons are excited or measured with Raman or infrared spectroscopy, however, which makes them pick up a tiny, but nonzero, wavevector perpendicular to the plane of circular polarization. Accordingly, the phonons obtain a helical structure, making them chiral.

ACKNOWLEDGMENTS

We thank Sebastian Stepanow (ETH Zurich), Xiaoqin (Elaine) Li, David Lujan, and Jeongheon Choe for useful discussions. This research was primarily supported by the National Science Foundation through the Center for Dynamics and Control of Materials: an NSF MRSEC under Cooperative Agreement No. DMR-1720595. G.A.F. acknowledges additional support from NSF DMR-2114825 and from the Alexander von Humboldt Foundation. D.M.J. acknowledges support from Tel Aviv University.

APPENDIX A: DERIVATION OF THE PHONON ZEEMAN SPLITTING AND EFFECTIVE PHONON MAGNETIC MOMENTS

In this section, we provide more details on the derivations of the equations in the main text. We begin by considering a degenerate phonon mode with two components that is described by the Hamiltonian

$$H_{ph} = \omega_0(a^\dagger a + b^\dagger b). \tag{A1}$$

We only consider phonon modes near the Brillouin zone center and can accordingly drop the momentum dependence in the phonon operators and energies. In order to account for the effect of orbital-lattice coupling on the phonon spectrum, we use a Green's function formalism. For the noninteracting system, the Green's function matrix is given by

$$\mathbf{D}_0(\omega) = \begin{pmatrix} D_0^{aa}(\omega) & 0 \\ 0 & D_0^{bb}(\omega) \end{pmatrix}, \tag{A2}$$

where the components are given by

$$D_0^{aa}(\omega) = D_0^{bb}(\omega) = \frac{2\omega_0}{\omega^2 - \omega_0^2}. \tag{A3}$$

The phonon frequency ω_0 can be trivially retrieved by solving $\mathrm{Det}(\mathbf{D}_0^{-1}(\omega)) = 0$. We obtain these Green's functions from the Fourier transform of time-dependent phonon propagators,

$$D_0^{aa}(t-t') = -i\theta(t-t')\,\langle 0|\,|A(t)A(t')\,|0\rangle - i\theta(t'-t)\,\langle 0|\,A(t')A(t)\,|0\rangle\,, \tag{A4}$$

$$D_0^{bb}(t-t') = -i\theta(t-t')\,\langle 0|\,|B(t)B(t')\,|0\rangle - i\theta(t'-t)\,\langle 0|\,B(t')B(t)\,|0\rangle\,, \tag{A5}$$

where $A(t) = a(t) + a^\dagger(t)$ and $B(t) = b(t) + b^\dagger(t)$ with $a(t) = ae^{-i\omega_0 t}$ and $b_k(t) = be^{-i\omega_0 t}$.

We next consider the electronic Hamiltonian, which can be expressed in second quantization as

$$H_{el} = \sum_{i=1}^{4} \varepsilon_i c_i^\dagger c_i, \tag{A6}$$

where $c_i^\dagger$ and c_i are the creation and annihilation operators for electrons in state i on the magnetic ion. Their Green's functions read

$$G_0^{ii}(t-t') = -i\langle 0|\mathcal{T}[c_i(t)c_i^\dagger(t')]|0\rangle = -i[\theta(t-t')\langle 0|c_i(t)c_i^\dagger(t')|0\rangle - \theta(t'-t)\langle 0|c_i^\dagger(t')c_i(t)|0\rangle], \tag{A7}$$

where the time-dependent operators are given by

$$c_i(t) = e^{i\varepsilon_i c_i^\dagger c_i t} c_i e^{-i\varepsilon_i c_i^\dagger c_i t} = e^{-i\varepsilon_i t} c_i. \tag{A8}$$

We can therefore write the Green's function as

$$G_0^{ii}(t-t') = -i[\theta(t-t')(1-f_i) - \theta(t'-t)f_i]e^{-i\varepsilon_i(t-t')}, \tag{A9}$$

where $f_i = \langle 0|c_i^\dagger c_i|0\rangle$ is the occupation number for state i, given by the Fermi-Dirac distribution. A Fourier transform of this expression yields

$$G_0^{ii}(\omega) = \frac{1-f_i}{\omega - \varepsilon_i + i\eta} + \frac{f_i}{\omega - \varepsilon_i - i\eta}. \tag{A10}$$

The orbit-lattice interaction of Eqs. (9) and (11) from the main text can therefore be expressed in second quantization as

$$H_{el-ph} = V^a + V^b, \tag{A11}$$

where

$$V^a = \sum_{i,j} g(a^\dagger + a)\Gamma^a_{ij} = g(a^\dagger + a)(c_3^\dagger c_1 + c_1^\dagger c_3) - g(a^\dagger + a)(c_4^\dagger c_2 + c_2^\dagger c_3), \tag{A12}$$

$$V^b = \sum_{i,j} g(a^\dagger + a)\Gamma^a_{ij} = ig(b^\dagger + b)(c_3^\dagger c_1 - c_1^\dagger c_3) + ig(b^\dagger + b)(c_4^\dagger c_2 - c_4^\dagger c_2). \tag{A13}$$

Including the orbit-lattice interaction, the interacting phonon propagator $\mathbf{D}$, and electronic propagator $\mathbf{G}$, are given by

$$\mathbf{D}(q,\omega) = D_0(q,\omega) + D_0(q,\omega)\mathbf{\Pi}(q,\omega)\mathbf{D}(q,\omega), \tag{A14}$$

where $\mathbf{\Pi}(q,\omega) = D_0^{-1} - \mathbf{D}^{-1}$ is the phonon self energy (the main quantity of interest for us), as well as

$$\mathbf{G}(q,\omega) = G_0(q,\omega) + G_0(q,\omega)\mathbf{\Sigma}(q,\omega)\mathbf{G}(q,\omega). \tag{A15}$$

In a perturbative treatment, $\mathbf{\Pi}$ and $\mathbf{\Sigma}$ can be calculated from noninteracting Green's functions. The full expression is given by

$$\begin{pmatrix} \mathbf{D}^{aa} & \mathbf{D}^{ab} \\ \mathbf{D}^{ba} & \mathbf{D}^{bb} \end{pmatrix} = \begin{pmatrix} D_0^{aa} & D_0^{ab} \\ D_0^{ba} & D_0^{bb} \end{pmatrix} + \begin{pmatrix} D_0^{aa} & D_0^{ab} \\ D_0^{ba} & D_0^{bb} \end{pmatrix} \mathbf{\Pi} \begin{pmatrix} \mathbf{D}^{aa} & \mathbf{D}^{ab} \\ \mathbf{D}^{ba} & \mathbf{D}^{bb} \end{pmatrix}, \tag{A16}$$

where the self-energy term is given by

$$\mathbf{\Pi} = \begin{pmatrix} \mathbf{\Pi}^{aa}_{13} + \mathbf{\Pi}^{aa}_{31} + \mathbf{\Pi}^{aa}_{24} + \mathbf{\Pi}^{aa}_{42} & \mathbf{\Pi}^{ab}_{13} + \mathbf{\Pi}^{ab}_{31} + \mathbf{\Pi}^{ab}_{24} + \mathbf{\Pi}^{ab}_{42} \\ \mathbf{\Pi}^{ba}_{13} + \mathbf{\Pi}^{ba}_{31} + \mathbf{\Pi}^{ba}_{24} + \mathbf{\Pi}^{ba}_{42} & \mathbf{\Pi}^{bb}_{13} + \mathbf{\Pi}^{bb}_{31} + \mathbf{\Pi}^{bb}_{24} + \mathbf{\Pi}^{bb}_{42} \end{pmatrix}. \tag{A17}$$

We now approximate this term with its noninteracting value,

$$\mathbf{\Pi}^{\alpha\chi}_{ij}(\omega) \approx \Pi^{\alpha\chi}_{ij}(\omega) = i\int d\omega' G_0^{ii}(\omega+\omega')G_0^{jj}(\omega')\Gamma^\alpha_{ij}\Gamma^\chi_{ji}. \tag{A18}$$

Together with the frequency-dependent electronic Green's function,

$$G_0^{ii}(\omega) = \frac{1-f_i}{\omega - \varepsilon_i + i\eta} + \frac{f_i}{\omega - \varepsilon_i - i\eta}, \tag{A19}$$

and using Eqs. (A12) and (A13) to write down $\Gamma^a_{13} = \Gamma^a_{31} = -\Gamma^a_{24} = -\Gamma^a_{42} = g$ and $\Gamma^b_{13} = -\Gamma^b_{31} = \Gamma^b_{24} = -\Gamma^b_{42} = ig$,

$$\int d\omega' G_0^{ii}(\omega+\omega')G_0^{jj}(\omega') = \int d\omega' \left(\frac{1-f_i}{\omega+\omega'-\varepsilon_i+i\eta} + \frac{f_i}{\omega+\omega'-\varepsilon_i-i\eta}\right)\left(\frac{1-f_j}{\omega'-\varepsilon_j+i\eta} + \frac{f_j}{\omega'-\varepsilon_j-i\eta}\right) \tag{A20}$$

$$= \int d\omega' \left[\left(\frac{(1-f_i)(1-f_j)}{(\omega+\omega'-\varepsilon_i+i\eta)(\omega'-\varepsilon_j+i\eta)}\right) + \left(\frac{(1-f_i)f_j}{(\omega+\omega'-\varepsilon_i+i\eta)(\omega'-\varepsilon_j-i\eta)}\right)\right] \tag{A21}$$

$$+ \int d\omega' \left[\left(\frac{f_i(1-f_j)}{(\omega+\omega'-\varepsilon_i-i\eta)(\omega'-\varepsilon_j+i\eta)}\right) + \left(\frac{f_i f_j}{(\omega+\omega'-\varepsilon_i-i\eta)(\omega'-\varepsilon_j-i\eta)}\right)\right] \tag{A22}$$

We utilize the relation $\lim_{\eta\to 0}\frac{1}{x+i\eta} = P(\frac{1}{x}) + i\pi\delta(x)$ and obtain

$$\int d\omega' \left[\left(\frac{(1-f_i)(1-f_j)}{(\omega+\omega'-\varepsilon_i+i\eta)(\omega'-\varepsilon_j+i\eta)}\right)\right] = \frac{(1-f_i)(1-f_j)}{\omega-\varepsilon_{ij}}\int d\omega'\left(\frac{1}{\omega'-\varepsilon_j+i\eta} - \frac{1}{\omega+\omega'-\varepsilon_i+i\eta}\right)$$
$$= 0, \tag{A23}$$

$$\int d\omega' \left[\left(\frac{(1-f_i)f_j}{(\omega+\omega'-\varepsilon_i+i\eta)(\omega'-\varepsilon_j-i\eta)}\right)\right] = \frac{(1-f_i)f_j}{\omega-\varepsilon_{ij}+2i\eta}\int d\omega'\left(\frac{1}{\omega'-\varepsilon_j-i\eta} - \frac{1}{\omega+\omega'-\varepsilon_i+i\eta}\right)$$
$$= -i2\pi\frac{(1-f_i)f_j}{\omega-\varepsilon_{ij}+2i\eta}, \tag{A24}$$

$$\int d\omega' \left[\left(\frac{f_i(1-f_j)}{(\omega+\omega'-\varepsilon_i+i\eta)(\omega'-\varepsilon_j+i\eta)}\right)\right] = \frac{f_i(1-f_j)}{\omega-\varepsilon_{ij}-2i\eta}\int d\omega'\left(\frac{1}{\omega'-\varepsilon_j+i\eta} - \frac{1}{\omega+\omega'-\varepsilon_i-i\eta}\right),$$
$$= i2\pi\frac{f_i(1-f_j)}{\omega-\varepsilon_{ij}-2i\eta} \tag{A25}$$

$$\int d\omega' \left[\left(\frac{f_i f_j}{(\omega + \omega' - \varepsilon_i - i\eta)(\omega' - \varepsilon_j - i\eta)} \right) \right] = \frac{f_i f_j}{\omega - \varepsilon_{ij}} \int d\omega' \left(\frac{1}{\omega' - \varepsilon_j - i\eta} - \frac{1}{\omega + \omega' - \varepsilon_i - i\eta} \right) = 0, \tag{A26}$$

as well as

$$\int d\omega' G_0^{ii}(\omega + \omega') G_0^{jj}(\omega') = -i2\pi \frac{(1 - f_i) f_j}{\omega - \varepsilon_{ij} + 2i\eta} + i2\pi \frac{f_i (1 - f_j)}{\omega - \varepsilon_{ij} - 2i\eta}. \tag{A27}$$

In the limit $\eta \to 0$, this expression becomes

$$\int d\omega' G_0^{ii}(\omega + \omega') G_0^{jj}(\omega') = i2\pi \frac{f_i - f_j}{\omega - \varepsilon_{ij}}. \tag{A28}$$

This allows us to obtain closed forms for the components of the self energy,

$$\Pi_{13}^{aa} + \Pi_{31}^{aa} = \Pi_{13}^{bb} + \Pi_{31}^{bb} = 2\pi g^2 (f_1 - f_3) \left(\frac{1}{\omega - \varepsilon_{13}} - \frac{1}{\omega - \varepsilon_{31}} \right) = 2\pi \frac{2g^2 (f_1 - f_3) \varepsilon_{13}}{\omega^2 - \varepsilon_{31}^2}, \tag{A29}$$

$$\Pi_{24}^{aa} + \Pi_{42}^{aa} = \Pi_{24}^{bb} + \Pi_{42}^{bb} = 2\pi g^2 (f_2 - f_4) \left(\frac{1}{\omega - \varepsilon_{24}} - \frac{1}{\omega - \varepsilon_{42}} \right) = 2\pi \frac{2g^2 (f_2 - f_4) \varepsilon_{24}}{\omega^2 - \varepsilon_{42}^2}, \tag{A30}$$

$$\Pi_{13}^{ab} + \Pi_{31}^{ab} = -\left(\Pi_{13}^{ba} + \Pi_{31}^{ba} \right) = -2\pi i g^2 (f_1 - f_3) \left(\frac{1}{\omega - \varepsilon_{13}} + \frac{1}{\omega - \varepsilon_{31}} \right) = 2\pi \frac{-2ig^2 (f_1 - f_3) \omega}{\omega^2 - \varepsilon_{31}^2}, \tag{A31}$$

$$\Pi_{24}^{ab} + \Pi_{42}^{ab} = -\left(\Pi_{24}^{ba} + \Pi_{42}^{ba} \right) = 2\pi i g^2 (f_2 - f_4) \left(\frac{1}{\omega - \varepsilon_{13}} + \frac{1}{\omega - \varepsilon_{31}} \right) = 2\pi \frac{2ig^2 (f_2 - f_4) \omega}{\omega^2 - \varepsilon_{42}^2}. \tag{A32}$$

Inserting these expressions into Eq. (A16), we get

$$\mathbf{D}^{-1} = \begin{pmatrix} \frac{\omega^2 - \omega_0^2}{2\omega_0} - \tilde{g}^2 \left(\frac{f_1 \Delta_1}{\omega^2 - \Delta_1^2} + \frac{f_2 \Delta_2}{\omega^2 - \Delta_2^2} \right) & i\tilde{g}^2 \left(-\frac{f_1 \omega}{\omega^2 - \Delta_1^2} + \frac{f_2 \omega}{\omega^2 - \Delta_2^2} \right) \\ -i\tilde{g}^2 \left(-\frac{f_1 \omega}{\omega^2 - \Delta_1^2} + \frac{f_2 \omega}{\omega^2 - \Delta_2^2} \right) & \frac{\omega^2 - \omega_0^2}{2\omega_0} - \tilde{g}^2 \left(\frac{f_1 \Delta_1}{\omega^2 - \Delta_1^2} + \frac{f_2 \Delta_2}{\omega^2 - \Delta_2^2} \right) \end{pmatrix}, \tag{A33}$$

where $\tilde{g}^2 = 4\pi g^2$, $\Delta_1 = \varepsilon_{31}$, $\Delta_2 = \varepsilon_{42}$ and we assume the excited state to be unoccupied, $f_3 = f_4 = 0$. The modified energies can then be obtained by solving $\mathrm{Det}(\mathbf{D}^{-1}) = 0$. The result of this equation depends on the application of a magnetic field, and we consider two cases.

Case 1. $B = 0$. Here, $f_1 = f_2 = f_0/2$ and $\Delta_1 = \Delta_2 = \Delta$. In this scenario, the off-diagonal term in $\mathbf{D}^{-1}$ is zero and the evaluation of $\mathrm{Det}(\mathbf{D}^{-1}(\omega)) = 0$ reduces to

$$\left(\omega^2 - \omega_0^2 \right) (\omega^2 - \Delta^2) - 2\tilde{g}^2 f_0 \omega_0 \Delta = 0, \tag{A34}$$

$$\left(\omega^2 - \omega_0^2 \right) (\omega^2 - \Delta^2) - 2\tilde{g}^2 f_0 \omega_0 \Delta = 0, \tag{A35}$$

which have identical solutions, indicating the doubly degenerate nature of phonon and electronic excitations. The solutions corresponding to the phonon and electronic excitation branches are respectively given by

$$\Omega_{ph} \equiv \omega_{ph}(B = 0) = \left(\frac{\omega_0^2 + \Delta^2}{2} + \sqrt{\left(\frac{\omega_0^2 - \Delta^2}{2} \right)^2 + 2\tilde{g}^2 f_0 \omega_0 \Delta} \right)^{1/2}, \tag{A36}$$

$$\Omega_{el} \equiv \omega_{el}(B = 0) = \left(\frac{\omega_0^2 + \Delta^2}{2} - \sqrt{\left(\frac{\omega_0^2 - \Delta^2}{2} \right)^2 + 2\tilde{g}^2 f_0 \omega_0 \Delta} \right)^{1/2}. \tag{A37}$$

This coupling modifies the phonon and electronic excitation energies but does not lift the degeneracy of two excitations. However, if the bare frequencies for two excitations are close, then even a weak orbit-lattice coupling term can introduce significant mixing and the excitations are no longer purely phononic or electronic in nature. We have focused only on the off-resonant case where these aspects can be safely ignored.

Case 2. $B \neq 0$. We next apply an external magnetic field, $\mathbf{B} = B\hat{\mathbf{z}}$, which lifts the degeneracies of the Kramers doublets, $\varepsilon_{12} \neq 0$ and $\varepsilon_{34} \neq 0$. This subsequently modifies the electronic transition energies as

$$\Delta_1 = \Delta - \gamma B, \quad \Delta_2 = \Delta + \gamma B, \tag{A38}$$

where $\gamma = \mu_{ex}^{el} - \mu_{gs}^{el}$ depends on the magnetic moment of the ground- and excited-state doublets. Lifting the degeneracy of the ground-state doublet leads to asymmetric populations of the ground-state energy levels, $f_{12} \neq 0$. Accordingly, the secular equation, $\mathrm{Det}(\mathbf{D}^{-1}(\omega)) = 0$ for $\mathbf{D}^{-1}$ given by Eq. (A33) becomes

$$\left(\omega^2 - \omega_0^2\right)\left(\omega^2 - \Delta^2\right) - 2\tilde{g}^2 f_0 \omega_0 \Delta + 2\omega\left(B\gamma\left(\omega^2 - \omega_0^2\right) + \tilde{g}^2 \omega_0 f_{21}\right) + \gamma B\left(\gamma B\left(\omega^2 - \omega_0^2\right) + 2\tilde{g}^2 \omega_0 f_{21}\right) = 0, \tag{A39}$$

$$\left(\omega^2 - \omega_0^2\right)\left(\omega^2 - \Delta^2\right) - 2\tilde{g}^2 f_0 \omega_0 \Delta - 2\omega\left(B\gamma\left(\omega^2 - \omega_0^2\right) + \tilde{g}^2 \omega_0 f_{21}\right) + \gamma B\left(\gamma B\left(\omega^2 - \omega_0^2\right) + 2\tilde{g}^2 \omega_0 f_{21}\right) = 0. \tag{A40}$$

These two equations are not equivalent and there is a term linear in ω that indicates a frequency splitting of phonon and electronic excitations. Given that the orbit-lattice coupling is weak and the electronic excitations are off-resonant from phonons, we can assume that phonon energies are modified only slightly and have the following form:

$$w_{ph}^{\pm} = \Omega_{ph}(1 \mp \eta), \tag{A41}$$

$$w_{el}^{\pm} = \Omega_{el}(1 \mp \epsilon). \tag{A42}$$

For the case of a paramagnetic system, the population difference is given by

$$f_{21} = -\tanh\left(\frac{\mu_{gs}^{el} B}{k_B T}\right). \tag{A43}$$

where μ_{gs}^{el} is the magnetic moment of ground-state manifold. We can plug the above equations into Eq. (A39) and Eq. (24) in order to obtain

$$\Omega_{ph}\eta = \frac{\gamma B\left(\Omega_+^2 - \omega_0^2\right) + \tilde{g}^2 \omega_0 f_{21}}{\Omega_{ph}^2 - \Omega_{el}^2 + \gamma^2 B^2} = \frac{\gamma B\left(\Omega_+^2 - \omega_0^2\right) + \tilde{g}^2 \omega_0 \tanh\left(\frac{\mu_{gs}^{el} B}{k_B T}\right)}{\sqrt{\left(\omega_0^2 - \Delta^2\right)^2 + 8\tilde{g}^2 f_0 \omega_0 \Delta} + \gamma^2 B^2}. \tag{A44}$$

For the off-resonant case, we can assume $|\Delta - \omega_0| \gg \gamma B$ and therefore neglect the linear B term in the numerator and the quadratic one in the denominator. The off-resonant case is a reasonable assumption, as $\gamma B \sim 0.5$ meV in strong magnetic fields of $B = 10$ T, whereas often $|\Delta - \omega_0| > 10$ meV. As a result, the splitting of the phonon frequencies can be written as

$$\frac{\omega_{ph}^{+} - \omega_{ph}^{-}}{\omega_{ph}(B=0)} \approx \frac{2\tilde{g}^2}{\sqrt{\left(\omega_0^2 - \Delta^2\right)^2 + 8\tilde{g}^2 f_0 \omega_0 \Delta}} \tanh\left(\frac{\mu_{gs}^{el} B}{k_B T}\right), \tag{A45}$$

which retrieves the early result by Thalmeier and Fulde [48].

APPENDIX B: ORBIT-LATTICE COUPLING OF THE E_{2g} MODES IN $CeCl_3$

The orbital-lattice coupling is evaluated by expanding the Coulomb potential in lattice displacement u_n,

$$V(\mathbf{R}_n, \mathbf{r}) = \frac{e^2}{4\pi\epsilon_0} \frac{1}{|\mathbf{R}_n - \mathbf{r}|}, \tag{B1}$$

where $\mathbf{R}_n = \mathbf{R}_{0,n} + \mathbf{u}_n$. We use Mathematica to perform a series expansion in u_n and different components of $\mathbf{r}$. This function can directly evaluate the following derivatives:

$$\partial_{u_n^\alpha} \partial_{r^\beta} \partial_{r^\gamma} \left(\frac{1}{|\mathbf{R}_n - \mathbf{r}|}\right)\Bigg|_{\mathbf{R}_n = \mathbf{R}_{0,n}, \mathbf{r}=0} \tag{B2}$$

when numerical values of $\mathbf{R}_{0,n}$ are provided.

As discussed in main text, the phonon lowers the symmetry around the magnetic ion and for the lattice distortion induced by E_{1g} phonon, the first order term for the change in Coulomb potential is given by

$$V(E_{1g}(a)) = [-0.06xz + 0.16yz]Q_a \frac{\mathrm{eV}}{\text{Å}^3\sqrt{\mathrm{amu}}}, \tag{B3}$$

$$V(E_{1g}(b)) = [0.16xz + 0.06yz]Q_b \frac{\mathrm{eV}}{\text{Å}^3\sqrt{\mathrm{amu}}}. \tag{B4}$$

Now, we can express $xz = r^2 \sin\theta\cos\theta\cos\phi$ and $yz = r^2\sin\theta\cos\theta\cos\phi$ in spherical coordinates. The electronic states on Ce^{3+} ion can be written in terms of $|L = 3, m = m_l\rangle$, which have wavefunction $\langle r|L = 3, m = m_l\rangle = R(r)Y_3^{m_l}(\theta,\phi)$. This allows us to calculate the matrix elements between different $4f$ states and the only nonzero terms are given by

$$\langle m = \pm 3|xz|m = \pm 2\rangle = \mp\langle r^2\rangle\frac{1}{3\sqrt{6}}, \tag{B5}$$

$$\langle m = \pm 2|xz|m = \pm 1\rangle = \mp\langle r^2\rangle\frac{1}{3\sqrt{10}}, \tag{B6}$$

$$\langle m = \pm 1|xz|m = \pm 0\rangle = \mp\langle r^2\rangle\frac{1}{3\sqrt{75}}, \tag{B7}$$

$$\langle m = \pm 3|yz|m = \pm 2\rangle = \langle r^2\rangle\frac{i}{3\sqrt{6}}, \tag{B8}$$

$$\langle m = \pm 2|yz|m = \pm 1\rangle = \langle r^2\rangle\frac{i}{3\sqrt{10}}, \tag{B9}$$

$$\langle m = \pm 1|yz|m = 0\rangle = \langle r^2\rangle\frac{i}{3\sqrt{75}}. \tag{B10}$$

Using these values for states given in Eqs. (35)–(37), we obtain

$$H_1(xz) = -\frac{2}{7\sqrt{5}}\langle r^2\rangle\begin{pmatrix} & \left|\frac{5}{2},\pm\frac{5}{2}\right\rangle & \left|\frac{5}{2},\pm\frac{3}{2}\right\rangle \\ \left|\frac{5}{2}\pm\frac{5}{2}\right\rangle & 0 & \pm 1 \\ \left|\frac{5}{2},\pm\frac{3}{2}\right\rangle & \pm 1 & 0 \end{pmatrix}, \tag{B11}$$

$$H_1(yz) = \frac{2}{7\sqrt{5}}\langle r^2\rangle\begin{pmatrix} & \left|\frac{5}{2},\pm\frac{5}{2}\right\rangle & \left|\frac{5}{2},\pm\frac{3}{2}\right\rangle \\ \left|\frac{5}{2},\pm\frac{5}{2}\right\rangle & 0 & i \\ \left|\frac{5}{2},\pm\frac{3}{2}\right\rangle & -i & 0 \end{pmatrix}. \tag{B12}$$

Next, we use the same microscopic model to calculate the Zeeman effect for other phonons as well. Here, we consider E_{2g}^1 (12 meV) and E_{2g}^2 (21.5 meV) phonons of $CeCl_3$. The phonon eigenvectors are obtained from density functional theory [26]. As mentioned in the main text [Eq. (B1)], these lattice displacements perturb the CEF around the Ce^{3+} ions, and the resulting modifications can be described as

$$V\left(E_{2g}^1(a)\right) = [-0.05xy - 0.007(x^2 - y^2)]Q_a\,\text{eV}/(\text{Å}^2\sqrt{\text{amu}}), \tag{B13}$$

$$V\left(E_{2g}^1(b)\right) = [0.014xy - 0.025(x^2 - y^2)]Q_b\,\text{eV}/(\text{Å}^2\sqrt{\text{amu}}), \tag{B14}$$

$$V\left(E_{2g}^2(a)\right) = [0.08xy + 0.01(x^2 - y^2)]Q_a\,\text{eV}/(\text{Å}^2\sqrt{\text{amu}}), \tag{B15}$$

$$V\left(E_{2g}^2(b)\right) = [-0.02xy + 0.04(x^2 - y^2)]Q_b\,\text{eV}/(\text{Å}^2\sqrt{\text{amu}}), \tag{B16}$$

where $Q_{a,b}$ is the amplitude of the phonon mode. Using spherical harmonics, we express this perturbation in the basis of electronic states, using

$$\langle m = \pm 3|xy|m = \pm 1\rangle = \pm\langle r^2\rangle\frac{i}{3\sqrt{15}}, \tag{B17}$$

$$\langle m = \pm 2|xy|m = \pm 0\rangle = \pm\langle r^2\rangle\frac{\sqrt{2}i}{3\sqrt{15}}, \tag{B18}$$

$$\langle m = \pm 1|xy|m = \mp 1\rangle = \pm\langle r^2\rangle\frac{2i}{15}, \tag{B19}$$

$$\langle m = \pm 3|x^2 - y^2|m = \pm 1\rangle = \langle r^2\rangle\frac{2}{3\sqrt{15}}, \tag{B20}$$

$$\langle m = \pm 2|x^2 - y^2|m = \pm 0\rangle = \langle r^2\rangle\frac{\sqrt{8}}{3\sqrt{15}}, \tag{B21}$$

$$\langle m = \pm 1|x^2 - y^2|m = \mp 1\rangle = \langle r^2\rangle\frac{4}{15}, \tag{B22}$$

which results in

$$H_1(x^2-y^2) = -\frac{2\sqrt{2}}{7\sqrt{5}}\langle r^2\rangle \begin{pmatrix} & \left|\frac{5}{2},\frac{5}{2}\right\rangle & \left|\frac{5}{2},\frac{1}{2}\right\rangle \\ \left|\frac{5}{2},\frac{5}{2}\right\rangle & 0 & 1 \\ \left|\frac{5}{2},\frac{3}{2}\right\rangle & 1 & 0 \end{pmatrix}, \tag{B23}$$

$$H_1(x^2-y^2) = -\frac{2\sqrt{2}}{7\sqrt{5}}\langle r^2\rangle \begin{pmatrix} & \left|\frac{5}{2},-\frac{5}{2}\right\rangle & \left|\frac{5}{2},-\frac{1}{2}\right\rangle \\ \left|\frac{5}{2},-\frac{5}{2}\right\rangle & 0 & 1 \\ \left|\frac{5}{2},-\frac{1}{2}\right\rangle & 1 & 0 \end{pmatrix}, \tag{B24}$$

$$H_1(xy) = \frac{\sqrt{2}}{7\sqrt{5}}\langle r^2\rangle \begin{pmatrix} & \left|\frac{5}{2},\frac{5}{2}\right\rangle & \left|\frac{5}{2},\frac{1}{2}\right\rangle \\ \left|\frac{5}{2},\frac{5}{2}\right\rangle & 0 & i \\ \left|\frac{5}{2},\frac{1}{2}\right\rangle & -i & 0 \end{pmatrix}, \tag{B25}$$

$$H_1(xy) = \frac{\sqrt{2}}{7\sqrt{5}}\langle r^2\rangle \begin{pmatrix} & \left|\frac{5}{2},-\frac{5}{2}\right\rangle & \left|\frac{5}{2},-\frac{1}{2}\right\rangle \\ \left|\frac{5}{2},-\frac{5}{2}\right\rangle & 0 & -i \\ \left|\frac{5}{2},-\frac{1}{2}\right\rangle & i & 0 \end{pmatrix}, \tag{B26}$$

where $\langle r^2\rangle$ is mean-square radius for $4f$ orbitals. The form of the Hamiltonian is similar to what we obtained for the E_{1g} mode in the main text, except for the fact that the E_{2g} modes couple the electronic orbitals $|\pm 5/2\rangle$ with $|\pm 1/2\rangle$. This coupling results in a significant phonon Zeeman effect and leads to chiral phonons as shown in Fig. 5(c).

APPENDIX C: ORBITAL CONFIGURATION AND ORBITAL-LATTICE COUPLING IN $CoTiO_3$

The Co^{2+} is a $3d^3$ system with three unpaired spins and for a free ion, Hund's coupling dictates that the ground-state manifold has $L = 3, S = 3/2$ and thus 28 degenerate states. These twenty-eight states can be obtained from linear combinations of the following seven states ($m_S = +3/2$):

$$|L=3, m_L=3\rangle = d^\dagger_{2\uparrow} d^\dagger_{1\uparrow} d^\dagger_{0\uparrow} |0\rangle\,, \tag{C1}$$

$$|L=3, m_L=2\rangle = d^\dagger_{2\uparrow} d^\dagger_{1\uparrow} d^\dagger_{-1\uparrow} |0\rangle\,, \tag{C2}$$

$$|L=3, m_L=1\rangle = \frac{1}{\sqrt{5}}\left(\sqrt{3} d^\dagger_{2\uparrow} d^\dagger_{0\uparrow} d^\dagger_{-1\uparrow} + \sqrt{2} d^\dagger_{2\uparrow} d^\dagger_{1\uparrow} d^\dagger_{-2\uparrow}\right)|0\rangle\,, \tag{C3}$$

$$|L=3, m_L=0\rangle = \frac{1}{\sqrt{5}}\left(d^\dagger_{1\uparrow} d^\dagger_{0\uparrow} d^\dagger_{-1\uparrow} + 2 d^\dagger_{2\uparrow} d^\dagger_{0\uparrow} d^\dagger_{-2\uparrow}\right)|0\rangle\,, \tag{C4}$$

$$|L=3, m_L=-1\rangle = -\frac{1}{\sqrt{5}}\left(\sqrt{3} d^\dagger_{-2\uparrow} d^\dagger_{0\uparrow} d^\dagger_{1\uparrow} + \sqrt{2} d^\dagger_{-2\uparrow} d^\dagger_{-1\uparrow} d^\dagger_{2\uparrow}\right)|0\rangle\,, \tag{C5}$$

$$|L=3, m_L=-2\rangle = -d^\dagger_{-2\uparrow} d^\dagger_{-1\uparrow} d^\dagger_{1\uparrow} |0\rangle\,, \tag{C6}$$

$$|L=3, m_L=-3\rangle = -d^\dagger_{-2\uparrow} d^\dagger_{-1\uparrow} d^\dagger_{0\uparrow} |0\rangle\,, \tag{C7}$$

where $d^\dagger_{j\uparrow}$ creates a d-orbital state according to

$$d^\dagger_{j\uparrow}|0\rangle \equiv \left|L=2, m_l=j, S=\tfrac{1}{2}, m_s=+\tfrac{1}{2}\right\rangle. \tag{C8}$$

These seven states are split by the octahedral CEF of the ligand ions. This CEF effect can be incorporated by introducing the following term to the Hamiltonian:

$$H_{Oh} = \Delta_0\left(\mathcal{P}_{T_{2g}} - \tfrac{3}{2}\mathcal{P}_{E_g}\right), \tag{C9}$$

where $\mathcal{P}_{T_{2g}/E_g}$ is the projection operator on the T_{2g} and E_g d orbitals. In terms of creation and annihilation operators for d orbitals, this term can be expressed as follows:

$$H_{Oh} = \Delta_0 \sum_{\sigma=\uparrow,\downarrow}\left(d^\dagger_{xy,\sigma} d_{xy,\sigma} + d^\dagger_{yz,\sigma} d_{yz,\sigma} + d^\dagger_{xz,\sigma} d_{xz,\sigma} - \frac{3}{2} d^\dagger_{x^2-y^2,\sigma} d_{x^2-y^2,\sigma} - \frac{3}{2} d^\dagger_{z^2,\sigma} d_{z^2,\sigma}\right), \tag{C10}$$

which splits the seven-dimensional Hilbert space into four different manifolds. The ground-state sector is spanned by the following three states:

$$|\tilde{1}\rangle = \sqrt{\frac{3}{8}}\,|3,1\rangle + \sqrt{\frac{5}{8}}\,|3,-3\rangle\,, \tag{C11}$$

$$|\tilde{0}\rangle = -\,|3,0\rangle\,, \tag{C12}$$

$$|-\tilde{1}\rangle = \sqrt{\frac{3}{8}}\,|3,-1\rangle + \sqrt{\frac{5}{8}}\,|3,3\rangle\,, \tag{C13}$$

which we denote by T_{1g} in Fig. 8(b), and the other three-sectors (irrelevant for our calculations) are given by

$$\sqrt{\frac{5}{8}}\,|3,1\rangle - \sqrt{\frac{3}{8}}\,|3,-3\rangle\,, \tag{C14}$$

$$\sqrt{\frac{5}{8}}\,|3,-1\rangle - \sqrt{\frac{3}{8}}\,|3,3\rangle\,, \tag{C15}$$

$$\sqrt{\frac{1}{2}}\,|3,2\rangle + \sqrt{\frac{1}{2}}\,|3,-2\rangle\,, \tag{C16}$$

$$\sqrt{\frac{1}{2}}\,|3,2\rangle - \sqrt{\frac{1}{2}}\,|3,-2\rangle\,. \tag{C17}$$

As the crystal field splitting arising from the octahedral field in this case is of the order of 1 eV, we are going to focus only on the ground-state sector, which can be represented as an effective angular momentum, $l_{\text{eff}} = 1$, sector with $\vec{l} = -\frac{2}{3}\vec{L}$. Next, we take into account the effect of spin-orbit coupling,

$$H_{\text{SO}} = \tfrac{3}{2}\lambda\vec{l}\cdot\vec{S}, \tag{C18}$$

which splits the $l_{\text{eff}} = 1$ manifold further into the following manifolds:

(i) $j_{\text{eff}} = 5/2$:

$$\left|\frac{5}{2},\frac{5}{2}\right\rangle = \left|m_l = \tilde{1}, m_s = \frac{3}{2}\right\rangle, \tag{C19}$$

$$\left|\frac{5}{2},\frac{3}{2}\right\rangle = \sqrt{\frac{2}{5}}\left|m_l = \tilde{0}, m_s = \frac{3}{2}\right\rangle + \sqrt{\frac{3}{5}}\left|m_l = \tilde{1}, m_s = \frac{1}{2}\right\rangle, \tag{C20}$$

$$\left|\frac{5}{2},\frac{1}{2}\right\rangle = \frac{1}{\sqrt{10}}\left(\left|m_l = -\tilde{1}, m_s = \frac{3}{2}\right\rangle + \sqrt{6}\left|m_l = \tilde{0}, m_s = \frac{1}{2}\right\rangle + \sqrt{3}\left|m_l = \tilde{1}, m_s = -\frac{1}{2}\right\rangle\right), \tag{C21}$$

$$\left|\frac{5}{2},-\frac{1}{2}\right\rangle = \frac{1}{\sqrt{10}}\left(\left|m_l = \tilde{1}, m_s = -\frac{3}{2}\right\rangle + \sqrt{6}\left|m_l = \tilde{0}, m_s = -\frac{1}{2}\right\rangle + \sqrt{3}\left|m_l = -\tilde{1}, m_s = \frac{1}{2}\right\rangle\right), \tag{C22}$$

$$\left|\frac{5}{2},-\frac{3}{2}\right\rangle = \sqrt{\frac{2}{5}}\left|m_l = \tilde{0}, m_s = -\frac{3}{2}\right\rangle + \sqrt{\frac{3}{5}}\left|m_l = -\tilde{1}, m_s = -\frac{1}{2}\right\rangle, \tag{C23}$$

$$\left|\frac{5}{2},-\frac{5}{2}\right\rangle = \left|m_l = -\tilde{1}, m_s = -\frac{3}{2}\right\rangle. \tag{C24}$$

(ii) $j_{\text{eff}} = 3/2$:

$$\left|\frac{3}{2},\frac{3}{2}\right\rangle = \sqrt{\frac{3}{5}}\left|m_l = \tilde{0}, m_s = \frac{3}{2}\right\rangle - \sqrt{\frac{2}{5}}\left|m_l = \tilde{1}, m_s = \frac{1}{2}\right\rangle, \tag{C25}$$

$$\left|\frac{3}{2},\frac{1}{2}\right\rangle = \frac{1}{\sqrt{15}}\left(\sqrt{6}\left|m_l = -\tilde{1}, m_s = \frac{3}{2}\right\rangle + \left|m_l = \tilde{0}, m_s = \frac{1}{2}\right\rangle - \sqrt{8}\left|m_l = \tilde{1}, m_s = -\frac{1}{2}\right\rangle\right), \tag{C26}$$

$$\left|\frac{3}{2},-\frac{1}{2}\right\rangle = \frac{1}{\sqrt{15}}\left(\sqrt{6}\left|m_l = \tilde{1}, m_s = -\frac{3}{2}\right\rangle + \left|m_l = \tilde{0}, m_s = -\frac{1}{2}\right\rangle - \sqrt{8}\left|m_l = -\tilde{1}, m_s = \frac{1}{2}\right\rangle\right), \tag{C27}$$

$$\left|\frac{3}{2},-\frac{3}{2}\right\rangle = \sqrt{\frac{3}{5}}\left|m_l = \tilde{0}, m_s = -\frac{3}{2}\right\rangle - \sqrt{\frac{2}{5}}\left|m_l = -\tilde{1}, m_s = -\frac{1}{2}\right\rangle. \tag{C28}$$

(iii) $j_{\text{eff}} = 1/2$:

$$\left|\frac{1}{2},\frac{1}{2}\right\rangle = \frac{1}{\sqrt{6}}\left(\sqrt{3}\left|m_l = -\tilde{1}, m_s = \frac{3}{2}\right\rangle - \sqrt{2}\left|m_l = \tilde{0}, m_s = \frac{1}{2}\right\rangle + \left|m_l = \tilde{1}, m_s = -\frac{1}{2}\right\rangle\right), \tag{C29}$$

$$\left|\frac{1}{2},-\frac{1}{2}\right\rangle = \frac{1}{\sqrt{6}}\left(\sqrt{3}\left|m_l=\tilde{1}, m_s=-\frac{3}{2}\right\rangle - \sqrt{2}\left|m_l=\tilde{0}, m_s=-\frac{1}{2}\right\rangle + \left|m_l=-\tilde{1}, m_s=\frac{1}{2}\right\rangle\right). \tag{C30}$$

Trigonal distortion. In $CoTiO_3$, the octahedral cage is trigonally distorted, which reduces the Co^{2+} site symmetry from O_h to C_3. This distortion is significant and it introduces a perturbation of the form $\delta L^2_{z_{tr}}$ along the z direction of the trigonal coordinate system, which splits the $j_{\text{eff}} = 3/2$ and $j_{\text{eff}} = 5/2$ manifolds further, according to the expectation value of j_z, where z axis is parallel (antiparallel) to c axis for site A (B) of the Co^{2+} ions, as shown in Fig. 11. The two lower manifolds can still be characterized by $m_j = \pm 1/2$ and $m_j = \pm 3/2$ and are predominantly composed of $j_{\text{eff}} = 1/2$ and $j_{\text{eff}} = 3/2$, respectively.

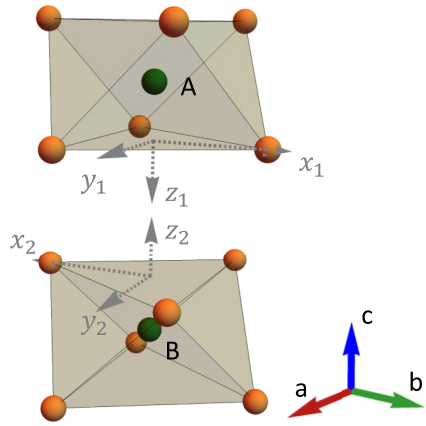

FIG. 11. Local coordinate system around each of the two Co^{2+} sites, A and B, of the rhombohedral unit cell.

Orbital-lattice coupling. In order to calculate the orbital-lattice coupling for Eqs. (61) and (62), we first express the electronic states $|1/2, \pm 1/2\rangle$ and $|3/2, \pm 3/2\rangle$ in terms of constituent d-orbital states in Eqs. (C1)–(C7), which in turn are expressed in the form of spherical harmonics and this gives

$$H_1(xz) = r_0^2 \frac{1}{70\sqrt{60}} \begin{pmatrix} & \left|\frac{1}{2}, \pm\frac{1}{2}\right\rangle & \left|\frac{3}{2}, \pm\frac{3}{2}\right\rangle \\ \left|\frac{1}{2}, \pm\frac{1}{2}\right\rangle & 0 & \pm 1 \\ \left|\frac{3}{2}, \pm\frac{3}{2}\right\rangle & \pm 1 & 0 \end{pmatrix}, \tag{C31}$$

$$H_1(yz) = r_0^2 \frac{1}{70\sqrt{60}} \begin{pmatrix} & \left|\frac{1}{2}, \pm\frac{1}{2}\right\rangle & \left|\frac{3}{2}, \pm\frac{3}{2}\right\rangle \\ \left|\frac{1}{2}, \pm\frac{1}{2}\right\rangle & 0 & i \\ \left|\frac{3}{2}, \pm\frac{3}{2}\right\rangle & -i & 0 \end{pmatrix}, \tag{C32}$$

for different perturbations in the Coulomb potential.

[1] J. Zhang and R. Averitt, Dynamics and control in complex transition metal oxides, Annu. Rev. Mater. Res. **44**, 19 (2014).

[2] H. Zhu, J. Yi, M.-Y. Li, J. Xiao, L. Zhang, C.-W. Yang, R. A. Kaindl, L.-J. Li, Y. Wang, and X. Zhang, Observation of chiral phonons, Science **359**, 579 (2018).

[3] S. Streib, Difference between angular momentum and pseudoangular momentum, Phys. Rev. B **103**, L100409 (2021).

[4] K. Ishito, H. Mao, Y. Kousaka, Y. Togawa, S. Iwasaki, T. Zhang, S. Murakami, J.-i. Kishine, and T. Satoh, Truly chiral phonons in α-HgS, Nat. Phys. **19**, 35 (2023).

[5] H. Ueda, M. García-Fernández, S. Agrestini, C. P. Romao, J. van den Brink, N. A. Spaldin, K.-J. Zhou, and U. Staub, Chiral phonons in quartz probed by x-rays, Nature (London) **618**, 946 (2023).

[6] Y. T. Rebane, Faraday effect produced in the residual-ray region by the magnetic moment of an optical phonon in an ionic crystal, Sov. Phys. JETP **57**, 1356 (1983).

[7] D. M. Juraschek, M. Fechner, A. V. Balatsky, and N. A. Spaldin, Dynamical multiferroicity, Phys. Rev. Mater. **1**, 014401 (2017).

[8] D. M. Juraschek and N. A. Spaldin, Orbital magnetic moments of phonons, Phys. Rev. Mater. **3**, 064405 (2019).

[9] G. Xiong, H. Chen, D. Ma, and L. Zhang, Effective magnetic fields induced by chiral phonons, Phys. Rev. B **106**, 144302 (2022).

[10] B. Cheng, T. Schumann, Y. Wang, X. Zhang, D. Barbalas, S. Stemmer, and N. P. Armitage, A large effective phonon magnetic moment in a Dirac semimetal, Nano Lett. **20**, 5991 (2020).

[11] A. Baydin, F. G. G. Hernandez, M. Rodriguez-Vega, A. K. Okazaki, F. Tay, G. T. Noe, I. Katayama, J. Takeda, H. Nojiri, P. H. O. Rappl, E. Abramof, G. A. Fiete, and J. Kono, Magnetic control of soft chiral phonons in PbTe, Phys. Rev. Lett. **128**, 075901 (2022).

[12] A. Zabalo, C. E. Dreyer, and M. Stengel, Rotational g factors and Lorentz forces of molecules and solids from density functional perturbation theory, Phys. Rev. B **105**, 094305 (2022).

[13] S. G. Jeong, J. Kim, A. Seo, S. Park, H. Y. Jeong, Y. M. Kim, V. Lauter, T. Egami, J. H. Han, and W. S. Choi, Unconventional interlayer exchange coupling via chiral phonons in synthetic magnetic oxide heterostructures, Sci. Adv. **8**, eabm4005 (2022).

[14] C. Strohm, G. L. J. A. Rikken, and P. Wyder, Phenomenological evidence for the phonon Hall effect, Phys. Rev. Lett. **95**, 155901 (2005).

[15] L. Sheng, D. N. Sheng, and C. S. Ting, Theory of the phonon Hall effect in paramagnetic dielectrics, Phys. Rev. Lett. **96**, 155901 (2006).

[16] L. Zhang, J. Ren, J. S. Wang, and B. Li, Topological nature of the phonon Hall effect, Phys. Rev. Lett. **105**, 225901 (2010).

[17] G. Grissonnanche, A. Legros, S. Badoux, E. Lefrançois, V. Zatko, M. Lizaire, F. Laliberté, A. Gourgout, J. S. Zhou, S. Pyon, T. Takayama, H. Takagi, S. Ono, N. Doiron-Leyraud, and L. Taillefer, Giant thermal Hall conductivity in the pseudogap phase of cuprate superconductors, Nature (London) **571**, 376 (2019).

[18] G. Grissonnanche, S. Thériault, A. Gourgout, M. E. Boulanger, E. Lefrançois, A. Ataei, F. Laliberté, M. Dion, J. S. Zhou, S. Pyon *et al.*, Chiral phonons in the pseudogap phase of cuprates, Nat. Phys. **16**, 1108 (2020).

[19] S. Park and B. J. Yang, Phonon angular momentum Hall effect, Nano Lett. **20**, 7694 (2020).

[20] T. Saito, K. Misaki, H. Ishizuka, and N. Nagaosa, Berry phase of phonons and thermal Hall effect in nonmagnetic insulators, Phys. Rev. Lett. **123**, 255901 (2019).

[21] B. Flebus and A. H. MacDonald, Charged defects and phonon Hall effects in ionic crystals, Phys. Rev. B **105**, L220301 (2022).

[22] B. Flebus and A. H. MacDonald, The phonon Hall viscosity of ionic crystals, Phys. Rev. Lett. **131**, 236301 (2023).

[23] T. F. Nova, A. Cartella, A. Cantaluppi, M. Först, D. Bossini, R. V. Mikhaylovskiy, A. V. Kimel, R. Merlin, and A. Cavalleri, An effective magnetic field from optically driven phonons, Nat. Phys. **13**, 132 (2017).

[24] D. M. Juraschek and P. Narang, Shaken not strained, Nat. Phys. **16**, 900 (2020).

[25] D. M. Juraschek, D. S. Wang, and P. Narang, Sum-frequency excitation of coherent magnons, Phys. Rev. B **103**, 094407 (2021).

[26] D. M. Juraschek, T. Neuman, and P. Narang, Giant effective magnetic fields from optically driven chiral phonons in $4f$ paramagnets, Phys. Rev. Res. **4**, 013129 (2022).

[27] R. M. Geilhufe, V. Juričić, S. Bonetti, J.-X. Zhu, and A. V. Balatsky, Dynamically induced magnetism in $KTaO_3$, Phys. Rev. Res. **3**, L022011 (2021).

[28] R. M. Geilhufe, Dynamic electron-phonon and spin-phonon interactions due to inertia, Phys. Rev. Res. **4**, L012004 (2022).

[29] R. M. Geilhufe and W. Hergert, Electron magnetic moment of chiral phonons, Phys. Rev. B **107**, L020406 (2023).

[30] M. Basini, M. Pancaldi, B. Wehinger, M. Udina, V. Unikandanunni, T. Tadano, M. Hoffmann, A. Balatsky, and S. Bonetti, Terahertz electric-field-driven dynamical multiferroicity in $SrTiO_3$, Nature (London) **628**, 534 (2024).

[31] C. Davies, F. Fennema, A. Tsukamoto, I. Razdolski, A. Kimel, and A. Kirilyuk, Phononic switching of magnetization by the ultrafast Barnett effect, Nature (London) **628**, 540 (2024).

[32] J. Luo, T. Lin, J. Zhang, X. Chen, E. R. Blackert, R. Xu, B. I. Yakobson, and H. Zhu, Large effective magnetic fields from chiral phonons in rare-earth halides, Science **382**, 698 (2023).

[33] S. Zhang, Y. Pei, S. Hu, N. Wu, D.-Q. Chen, C. Lian, and S. Meng, Light-induced phonon-mediated magnetization in monolayer MoS_2, Chin. Phys. Lett. **40**, 077502 (2023).

[34] N. Shabala and R. M. Geilhufe, Phonon inverse Faraday effect from electron-phonon coupling, arXiv:2405.09538.

[35] J. Fransson, Chiral phonon induced spin polarization, Phys. Rev. Res. **5**, L022039 (2023).

[36] K. Kim, E. Vetter, L. Yan, C. Yang, Z. Wang, R. Sun, Y. Yang, A. H. Comstock, X. Li, J. Zhou *et al.*, Chiral-phonon-activated spin Seebeck effect, Nat. Mater. **22**, 322 (2023).

[37] X. Li, J. Zhong, J. Cheng, H. Chen, H. Wang, J. Liu, D. Sun, L. Zhang, and J. Zhou, Chiral phonon activated spin Seebeck effect in chiral materials, Sci. China Phys. Mech. Astron. **67**, 237511 (2024).

[38] D. Ceresoli, Berry phase calculations of the rotational and pseudorotational g-factor in molecules and solids, Ph.D. thesis, SISSA, Triete, 2002.

[39] M. Hamada, E. Minamitani, M. Hirayama, and S. Murakami, Phonon angular momentum induced by the temperature gradient, Phys. Rev. Lett. **121**, 175301 (2018).

[40] G. Schaack, Observation of circularly polarized phonon states in an external magnetic field, J. Phys. C: Solid State Phys. **9**, L297 (1976).

[41] G. Schaack, Magnetic field dependent splitting of doubly degenerate phonon states in anhydrous cerium-trichloride, Z. Physik B **26**, 49 (1977).

[42] D. Shin, H. Hübener, U. De Giovannini, H. Jin, A. Rubio, and N. Park, Phonon-driven spin-Floquet magneto-valleytronics in MoS_2, Nat. Commun. **9**, 638 (2018).

[43] F. G. Hernandez, A. Baydin, S. Chaudhary, F. Tay, I. Katayama, J. Takeda, H. Nojiri, A. K. Okazaki, P. H. Rappl, E. Abramof *et al.*, Observation of interplay between phonon chirality and electronic band topology, Sci. Adv. **9**, eadj4074 (2023).

[44] S. Sengupta, M. N. Y. Lhachemi, and I. Garate, Phonon magnetochiral effect of band-geometric origin in Weyl semimetals, Phys. Rev. Lett. **125**, 146402 (2020).

[45] C. Xiao, Y. Ren, and B. Xiong, Adiabatically induced orbital magnetization, Phys. Rev. B **103**, 115432 (2021).

[46] Y. Ren, C. Xiao, D. Saparov, and Q. Niu, Phonon magnetic moment from electronic topological magnetization, Phys. Rev. Lett. **127**, 186403 (2021).

[47] X.-W. Zhang, Y. Ren, C. Wang, T. Cao, and D. Xiao, Gate-tunable phonon magnetic moment in bilayer graphene, Phys. Rev. Lett. **130**, 226302 (2023).

[48] P. Thalmeier and P. Fulde, Optical phonons of Rare-Earth halides in a magnetic field, Z. Phys. B **26**, 323 (1977).

[49] P. Thalmeier and P. Fulde, Faraday and Cotton-Mouton effects for acoustic phonons in paramagnetic Rare Earth compounds, Z. Phys. B **29**, 299 (1978).

[50] K. Stevens, Matrix elements and operator equivalents connected with the magnetic properties of Rare Earth ions, Proc. Phys. Soc. A **65**, 209 (1952).

[51] L. Zhang and Q. Niu, Chiral phonons at high-symmetry points in monolayer hexagonal lattices, Phys. Rev. Lett. **115**, 115502 (2015).

[52] G. Schaack, Magnetic-field dependent phonon states in paramagnetic CeF_3, Solid State Commun. **17**, 505 (1975).

[53] J. Andriessen, P. Dorenbos, and C. W. E. van Eijk, *Ab initio* calculation of the contribution from anion dipole polarization and dynamic correlation to $4f-5d$ excitations of Ce^{3+} in ionic compounds, Phys. Rev. B **72**, 045129 (2005).

[54] D. Khomskii, K. Kugel, A. Sboychakov, and S. Streltsov, Role of local geometry in the spin and orbital structure of transition metal compounds, J. Exp. Theor. Phys. **122**, 484 (2016).

[55] J. B. Goodenough, Spin-orbit-coupling effects in transition-metal compounds, Phys. Rev. **171**, 466 (1968).

[56] B. Yuan, M. B. Stone, G.-J. Shu, F. C. Chou, X. Rao, J. P. Clancy, and Y.-J. Kim, Spin-orbit exciton in a honeycomb lattice magnet $CoTiO_3$: Revealing a link between magnetism in d- and f-electron systems, Phys. Rev. B **102**, 134404 (2020).

[57] B. Yuan, I. Khait, G.-J. Shu, F. C. Chou, M. B. Stone, J. P. Clancy, A. Paramekanti, and Y.-J. Kim, Dirac magnons in a

honeycomb lattice quantum *XY* magnet $CoTiO_3$, Phys. Rev. X **10**, 011062 (2020).

[58] M. Elliot, P. A. McClarty, D. Prabhakaran, R. Johnson, H. Walker, P. Manuel, and R. Coldea, Order-by-disorder from bond-dependent exchange and intensity signature of nodal quasiparticles in a honeycomb cobaltate, Nat. Commun. **12**, 3936 (2021).

[59] R. Dubrovin, N. Siverin, M. Prosnikov, V. Chernyshev, N. Novikova, P. Christianen, A. Balbashov, and R. Pisarev, Lattice dynamics and spontaneous magnetodielectric effect in ilmenite $CoTiO_3$, J. Alloys Compd. **858**, 157633 (2021).

[60] E. Kroumova, M. Aroyo, J. Perez-Mato, A. Kirov, C. Capillas, S. Ivantchev, and H. Wondratschek, Bilbao crystallographic server: Useful databases and tools for phase-transition studies, Ph. Transit. **76**, 155 (2003).

[61] R. D. Shannon, Revised effective ionic radii and systematic studies of interatomic distances in halides and chalcogenides, Acta Cryst. A **32**, 751 (1976).

[62] J. Bonini, S. Ren, D. Vanderbilt, M. Stengel, C. E. Dreyer, and S. Coh, Frequency splitting of chiral phonons from broken time-reversal symmetry in CrI_3, Phys. Rev. Lett. **130**, 086701 (2023).

[63] D. P. Landau, J. C. Doran, and B. E. Keen, Thermal and magnetic properties of $CeCl_3$, Phys. Rev. B **7**, 4961 (1973).

[64] L. J. Sandilands, Y. Tian, A. A. Reijnders, H.-S. Kim, K. W. Plumb, Y.-J. Kim, H.-Y. Kee, and K. S. Burch, Spin-orbit excitations and electronic structure of the putative Kitaev magnet $\alpha - RuCl_3$, Phys. Rev. B **93**, 075144 (2016).

[65] M. Takahashi, Half-filled Hubbard model at low temperature, J. Phys. C: Solid State Phys. **10**, 1289 (1977).

[66] N. S. Fedorova, A. Bortis, C. Findler, and N. A. Spaldin, Four-spin ring interaction as a source of unconventional magnetic orders in orthorhombic perovskite manganites, Phys. Rev. B **98**, 235113 (2018).

[67] S. Liu, A. Granados del Águila, D. Bhowmick, C. K. Gan, T. Thu Ha Do, M. A. Prosnikov, D. Sedmidubský, Z. Sofer, P. C. M. Christianen, P. Sengupta, and Q. Xiong, Direct observation of magnon-phonon strong coupling in two-dimensional antiferromagnet at high magnetic fields, Phys. Rev. Lett. **127**, 097401 (2021).

[68] D. Vaclavkova, M. Palit, J. Wyzula, S. Ghosh, A. Delhomme, S. Maity, P. Kapuscinski, A. Ghosh, M. Veis, M. Grzeszczyk, C. Faugeras, M. Orlita, S. Datta, and M. Potemski, Magnon polarons in the van der Waals antiferromagnet, Phys. Rev. B **104**, 134437 (2021).

[69] J. Cui, E. V. Boström, M. Ozerov, F. Wu, Q. Jiang, J.-H. Chu, C. Li, F. Liu, X. Xu, A. Rubio *et al.*, Chirality selective magnon-phonon hybridization and magnon-induced chiral phonons in a layered zigzag antiferromagnet, Nat. Commun. **14**, 3396 (2023).

[70] B. Ma, Z. D. Wang, and G. V. Chen, Chiral phonons induced from spin dynamics via magnetoelastic anisotropy, arXiv:2309.04064.

[71] T. Kahana, D. A. B. Lopez, and D. M. Juraschek, Light-induced weak ferromagnetism through nonlinear magnonic rectification, arXiv:2305.18656.